

Article

Synthesis Design of Electronegativity Dependent WO_3 and $\text{WO}_3 \cdot 0.33\text{H}_2\text{O}$ Materials for a Better Understanding of TiO_2/WO_3 Composites' Photocatalytic Activity

István Székely ^{1,2} , Endre-Zsolt Kedves ^{1,2,3} , Zsolt Pap ^{2,4,*} and Monica Baia ^{1,2,*} 

¹ Faculty of Physics, Babeş-Bolyai University, Mihail Kogălniceanu Str. 1, RO-400084 Cluj-Napoca, Romania; istvan.székely@ubbcluj.ro (I.S.); endre.kedves@ubbcluj.ro (E.-Z.K.)

² Interdisciplinary Research Institute on Bio-Nano-Sciences, Babeş-Bolyai University, Treboniu Laurian Str. 42, RO-400271 Cluj-Napoca, Romania

³ Department of Biosystems Engineering, Faculty of Engineering, University of Szeged, Moszkvai Bld. 9, HU-6725 Szeged, Hungary

⁴ Department of Applied and Environmental Chemistry, University of Szeged, Rerrich Béla Sqr. 1, HU-6720 Szeged, Hungary

* Correspondence: zsolt.pap@ubbcluj.ro (Z.P.); monica.baia@ubbcluj.ro (M.B.)

Abstract: The design of a semiconductor or a composite semiconductor system—with applications in materials science—is complex because its morphology and structure depend on several parameters. These parameters are the precursor type, solvent, pH of the solution, synthesis approach, or shaping agents. This study gives meaningful insight regarding the synthesis design of such WO_3 materials. By systematically alternating the precursor (sodium tungstate dihydrate—NWH, or ammonium tungstate hydrate—AMT), subsequently shaping the agents (halide salts— NaX , KX , or hydrohalic acids— HX ; $\text{X} = \text{F}^-$, Cl^- , Br^- , I^-), we have obtained WO_3 semiconductors by hydrothermal treatment, which in composite systems can enhance the commercial TiO_2 photocatalytic activity. We investigated three sample series: WO_3 -NWH- NaX / WO_3 -NWH- KX and, subsequently, WO_3 -AMT- HX . The presence of W^{+5} centers was evidenced by Raman and X-ray photoelectron spectroscopy. W^{+5} and W^{+6} species affected the band gap values of the NaX and KX series; a higher percentage of W^{+5} and, subsequently, W^{+6} caused a redshift, while, regarding the HX series, it led to a blue shift. Increased electronegativity of the halide anions has an unfavorable effect on the composites' photoactivity. In contrast, in the case of hydrohalic acids, it had a positive impact.



Citation: Székely, I.; Kedves, E.-Z.; Pap, Z.; Baia, M. Synthesis Design of Electronegativity Dependent WO_3 and $\text{WO}_3 \cdot 0.33\text{H}_2\text{O}$ Materials for a Better Understanding of TiO_2/WO_3 Composites' Photocatalytic Activity. *Catalysts* **2021**, *11*, 779. <https://doi.org/10.3390/catal11070779>

Academic Editor: Edward G. Gillan

Received: 3 June 2021

Accepted: 24 June 2021

Published: 27 June 2021

Publisher's Note: MDPI stays neutral with regard to jurisdictional claims in published maps and institutional affiliations.



Copyright: © 2021 by the authors. Licensee MDPI, Basel, Switzerland. This article is an open access article distributed under the terms and conditions of the Creative Commons Attribution (CC BY) license (<https://creativecommons.org/licenses/by/4.0/>).

Keywords: tungsten trioxide; electronegativity; morpho-structural properties; oxygen vacancies; surface defects; photocatalytic activity; synthesis design

1. Introduction

Tungsten trioxide (WO_3) is an extensively studied n-type semiconductor (SC) that has a broad application spectrum, including pigment in paints [1], gas sensors [2,3], and humidity sensors [4], or is an essential component in (photo) electrochromic devices [5–8]. It can also be employed as a photocatalyst on its own or in composites with other metal oxides [9–14], or with carbon-based materials [15]. Its band gap value is ≈ 2.6 eV, meaning a light absorption maximum at 480 nm. Furthermore, WO_3 is considered environmentally friendly and harmless [16].

Tungsten trioxide SCs can be synthesized via different methods, such as electrospinning [17,18], chemical vapor deposition [19,20], physical vapor deposition [21], ultrasonic spraying, laser pyrolysis [22,23], and hydro-/solvothermal crystallization [24–26].

Numerous WO_3 nanostructures were synthesized using hydrothermal crystallization, such as nanowires [27,28], nanorods [29,30], and nanofibers [31,32]. The morphology and structure of the WO_3 SCs can be influenced by the precursor's structure [33–35], synthesis method [36–38], solvent type [39], annealing time, and temperature [40,41].

A broad spectrum of techniques and methods is the key to designing the morphology and structure of materials. However, one of the most commonly employed methods implies the variation of the ionic strength of the synthesis mixture, or the replacement of the used salts' anions and cations based on their electronegativity, which was proven in the case of TiO_2 using NaCl [42] or NaCl/KCl salts in the synthesis mixture [43,44]. Furthermore, the effect of different zinc salts upon the synthesized ZnO nanoparticle morphology, crystal size, and antiseptic properties was also investigated [45,46] and also found to be valid in the case of NiO [47].

The effect of different salts (NH_4Cl , NH_4NO_3 , Li_2SO_4 , and Na_2SO_4) upon the WO_3 structure and morphology ascertained that, by microwave-assisted hydrothermal approach, hexagonal WO_3 nanowires could be obtained. When no salts were added during the synthesis, it yielded $\text{WO}_3 \cdot 0.33\text{H}_2\text{O}$, sequentially, by introducing ammonium salts (NH_4Cl , NH_4NO_3 , or $(\text{NH}_4)_2\text{SO}_4$) pure hexagonal WO_3 was obtained. The addition of lithium and sodium cations did not facilitate hexagonal WO_3 [48]. The addition of ammonium salts ($(\text{NH}_4)_2\text{SO}_4$, NH_4Cl , or NH_4NO_3) influenced the WO_3 structure and morphology; more precisely, 55% hexagonal and 45% orthorhombic WO_3 crystal phase composition was achieved, with slab-like morphology. In contrast, the addition of ammonium salts resulted in rod-like WO_3 semiconductors with a hexagonal crystal phase [49].

Although the effect of several anions and cations upon the morphological, structural, optical, and other significant characteristics of the semiconductors was studied, no relevant papers have yet been published to address the effect of different anions and cations (salts and hydrohalic acids) and, subsequently, their electronegativity, on the semiconductors' photocatalytic performance. Moreover, relevant studies concerning the effect of different anions and cations—electronegativity and ion mobility—on the photocatalytic activity of WO_3 have not yet been published.

Concerning this study, the synthesis of WO_3 materials was designed (Figure 1) from two different precursors via hydrothermal crystallization, introducing different salts/hydrohalic acids into the synthesis environment. The morphology, structure, and photocatalytic activity of the obtained compounds were studied. Additionally, TiO_2 - WO_3 composites were prepared to evaluate their photoactivity, and the activity–morphology–structure relationship was determined.

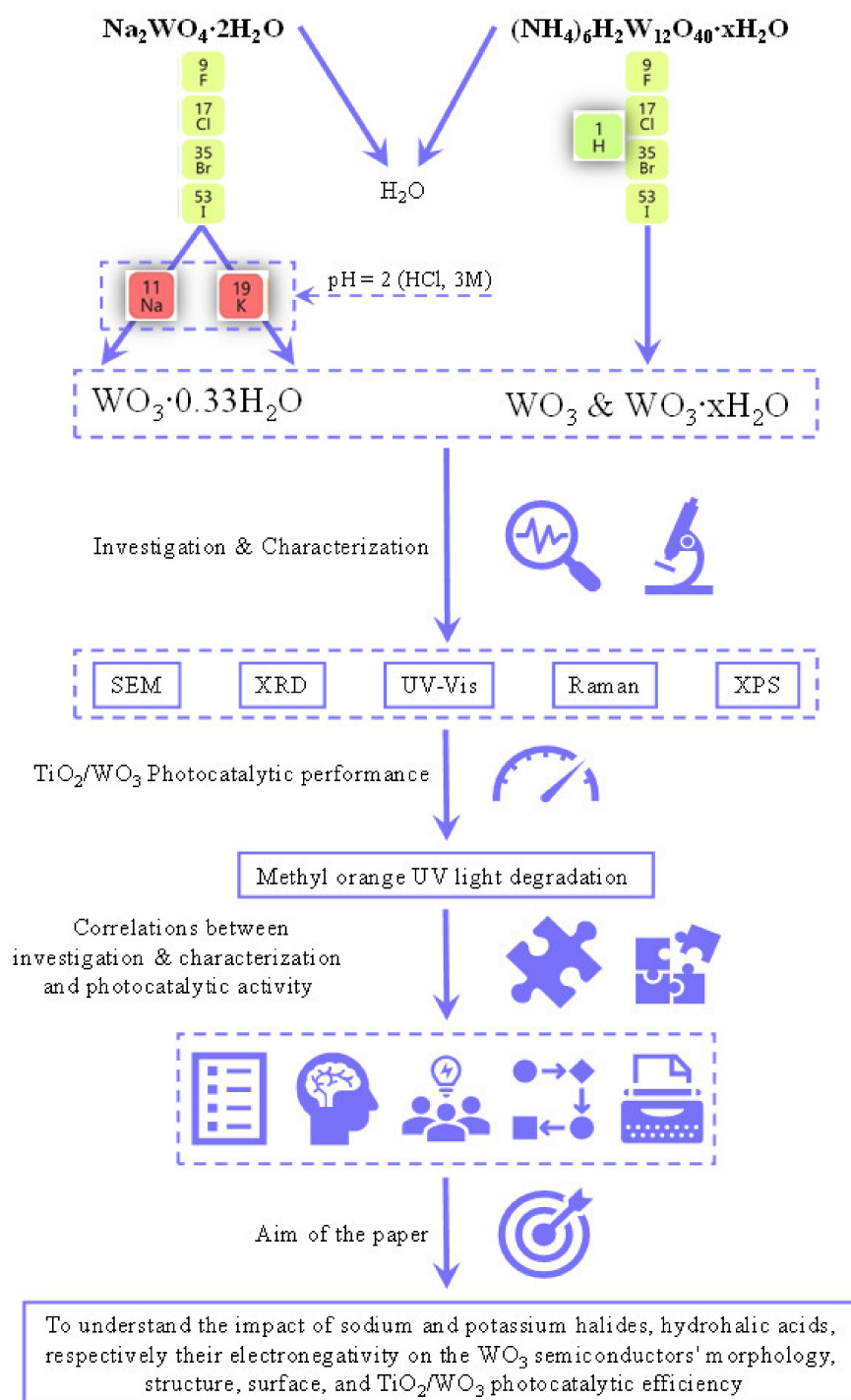


Figure 1. The research design of the proposed manuscript.

2. Results

2.1. The Morphology of the Semiconductors

Scanning electron microscopy was employed to evaluate the morphology of the synthesized semiconductors. In the case of the WO_3 -NWH-NaF semiconductors (Figure 2), bullet-like morphology can be observed, each with a size of 1–2 μm . Additionally, smaller cylinder-shaped nanocrystals were observed between 300–500 nm, and even smaller ones were observed between 50–200 nm, built up of/from very thin nanowires. WO_3 -NWH-NaCl crystals (Figure 2) showed fiber-like morphology. Their resultant length was 3–4 μm (constructed from ≈ 12 –14 nm size nanofibers). The morphology of crys-

tals from the samples $\text{WO}_3\text{-NWH-NaBr}$ and $\text{WO}_3\text{-NWH-NaI}$ was fiber-like (Figure 2, length = 1–2 μm /diameter \approx of 100 nm and 150 nm for $\text{WO}_3\text{-NWH-NaI}$). This morphological feature can also be observed in the case of the $\text{WO}_3\text{-NWH-NaCl}$ sample.

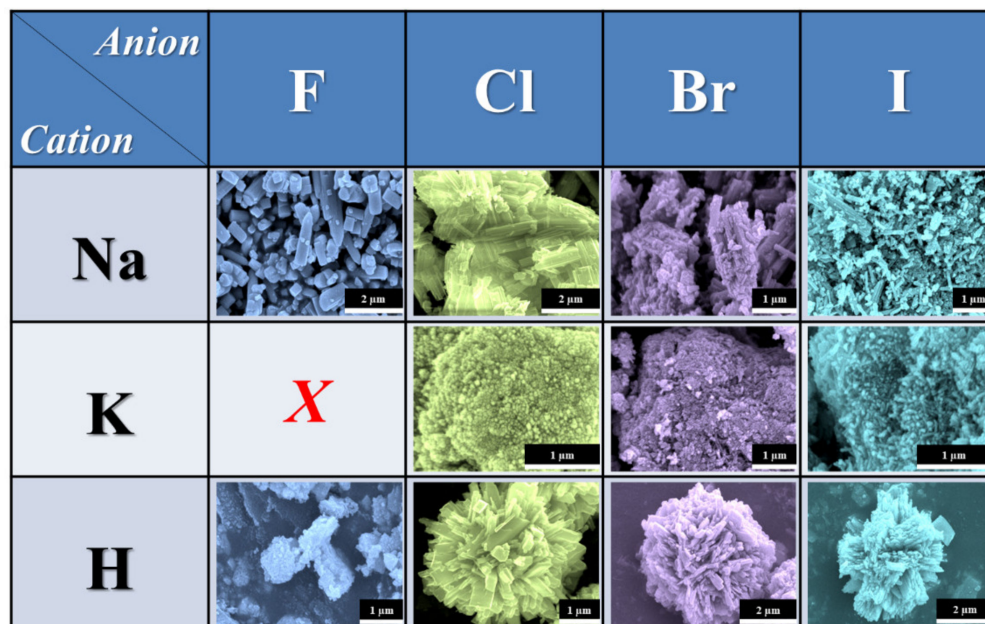


Figure 2. SEM micrographs of $\text{WO}_3\text{-NWH-NaX}$, $\text{WO}_3\text{-NWH-KX}$, and $\text{WO}_3\text{-AMT-HX}$ series.

Concerning $\text{WO}_3\text{-NWH-KCl}$ (Figure 2), nanocrystals with a wire-like morphology were obtained, which were randomly aggregated. Additionally, some very thin nanowires (40–50 nm) can be observed with various lengths (400–600 nm). $\text{WO}_3\text{-NWH-KBr}$ crystals were also wire-like (Figure 2), while the nanocrystals' size was between 50 and 100 nm. In comparison, $\text{WO}_3\text{-NWH-KI}$ presented wire/sheet-like crystals (50–100 nm, Figure 2).

In $\text{WO}_3\text{-AMT-HF}$, the observed morphology was slightly spherical (Figure 2). The aggregations were also present (below 1.0 μm , mainly between 0.1–1.0 μm). Besides the spherical crystals, a large number of undetermined crystal shapes were also noticed. It should be noted that smaller nanoplates (\approx 100–400 nm) can also be observed, which build up the larger-sized crystals layer by layer. The morphology of $\text{WO}_3\text{-AMT-HCl}$ was star-like. These entities' mean diameter was \approx 3–4 μm and consisted of microfibers of \approx 3–4 μm length, assembled from numerous smaller nanowires (10–15 nm). The morphology of $\text{WO}_3\text{-AMT-HBr}$ was similar to that of $\text{WO}_3\text{-AMT-HCl}$, and the stars measured 3–4 μm . Interestingly, $\text{WO}_3\text{-AMT-HI}$ showed the same star-like morphology, while their mean diameter was in the range of 2–3 μm . These stars were made up of \approx 2–4 μm lengths from microfibers and assembled from numerous smaller nanowires. High-resolution SEM micrographs have been added to the Supplementary Materials to present the above-mentioned shape-controlled WO_3 and $\text{WO}_3 \cdot 0.33\text{H}_2\text{O}$ nano- and microcrystals.

2.2. Optical Properties of the WO_3 Semiconductors and TiO_2/WO_3 Composite Systems

From the diffuse reflectance spectra of the materials, the optical properties were assessed. The reflectance spectra of each series and their corresponding composite systems can be found in the paper's Supplementary Materials section.

Regarding the band gap value of the synthesized SCs, no particular trend was observed between the anions/cations' effects and the band gap energy (Table 1). The highest and lowest values are marked in Table 1. The band gap values of the TiO_2/WO_3 composites compared with those of the counterpart WO_3 SCs have shown a blue shift caused by the high percentage of P25 (76%) in the composites. No trend was observed in the case of the composite systems. The synthesized WO_3 SCs and TiO_2/WO_3 composite systems also absorb the photons of UV and visible light regions. The various band gap values

in each series could mean that, although a high concentration of H^+ (acidic pH) was present, the samples' morphology and structure were more significantly influenced by the added halides, regarding the WO_3 -NWH-NaX and WO_3 -NWH-KX series. The presence of sodium/potassium halides and, subsequently, the hydrohalic acids, had an impact upon the morphology, structure, color, and band gap of the samples, which could mean, regarding all series, that the shaping agents and their electronegativity influenced the electrons' migration path, density, and mobility.

Table 1. Band gap values of the “bare” WO_3 semiconductors and TiO_2/WO_3 composite systems.

WO_3		TiO_2/WO_3	
Sample	Band Gap Value (eV)	Sample	Band Gap Value (eV)
WO_3 -NWH-NaF	2.95 ↑	WO_3 -NWH-NaF+P25	2.98
WO_3 -NWH-NaCl	2.69 ↓	WO_3 -NWH-NaCl+P25	2.97
WO_3 -NWH-NaBr	2.84	WO_3 -NWH-NaBr+P25	2.99
WO_3 -NWH-NaI	2.78	WO_3 -NWH-NaI+P25	3.04
WO_3 -NWH-KCl	2.64	WO_3 -NWH-KCl+P25	3.00
WO_3 -NWH-KBr	2.66 ↑	WO_3 -NWH-KBr+P25	3.02
WO_3 -NWH-KI	2.54 ↓	WO_3 -NWH-KI+P25	3.03
WO_3 -AMT-HF	2.94 ↑	WO_3 -AMT-HF+P25	3.01
WO_3 -AMT-HCl	2.25 ↓	WO_3 -AMT-HCl+P25	3.10
WO_3 -AMT-HBr	2.53	WO_3 -AMT-HBr+P25	2.78
WO_3 -AMT-HI	2.77	WO_3 -AMT-HI+P25	2.87

The highest ↓ and lowest ↑ value within a series.

The band gap values of the WO_3 -NWH-NaX and WO_3 -NWH-KX series (hexagonal crystal phase) were between 2.69 and 2.95 eV, sequentially 2.54 and 2.66 eV, whereas the literature provides values between 2.50 and 2.76 eV for the hexagonal crystal phase. Concerning the WO_3 -AMT-HX series, where monoclinic, hexagonal, and their mixed crystal phases were identified, the band gap values were between 2.25 and 2.94 eV (2.25 eV for 100% monoclinic crystal phase and 2.94 eV for 100% hexagonal crystal phase), whereas, in the literature, monoclinic WO_3 had shown band gap values between 2.64 and 2.85 eV; subsequently, the monoclinic and hexagonal mixture provided a 2.48 eV band gap [50–52]. Thus, overall, the band gap values of our samples only slightly overlap with the band gaps values found in the literature.

Moreover, for each sample, the conduction and valence band values were determined by applying Mulliken electronegativity theory (Table 2). To do this, the absolute electronegativity of WO_3 (6.59 eV) was taken into consideration. Because we investigated oxide materials, we relied on the work of Xu, Y.; Schoonen, M.A.; and Ali, H. et al. [53,54]. In order to calculate the semiconductors' conduction and valence bands, the following equations were used:

$$E_{CB} = X - 4.5 \text{ eV} - 0.5E_g \quad (1)$$

$$E_{VB} = E_{CB} + E_g, \quad (2)$$

where E_{CB} is the conduction band energy, X is the absolute electronegativity of the semiconductor, and 4.5 eV is the reduction potential of the normal hydrogen electrode (NHE). E_g is the semiconductors band gap value; consequently, E_{VB} is the valence band energy in eV. However, the accuracy of these calculations depends on many parameters, such as the piezoelectric point of the semiconductors, the pH of the suspension, and the dipole associated potential drop because these values are valid if the materials are in a vacuum [53,54]. The added halide salts/hydrohalic acids did not affect, in a systematic trend, the sample's conduction and valence bands; still, it should be mentioned that high elec-

tronegativity led to the lowest conduction and the highest valence band values in the $\text{WO}_3\text{-NWH-NaX}$ ($\text{WO}_3\text{-NWH-NaF}$ 0.62 eV; 3.57 eV) and $\text{WO}_3\text{-AMT-HX}$ ($\text{WO}_3\text{-AMT-HF}$ 0.62 eV; 3.56 eV) series.

Table 2. Conduction band and valence band values of the “bare” WO_3 composites.

Sample	E_g (eV)	E_{CB} (eV)	E_{VB} (eV)
$\text{WO}_3\text{-NWH-NaF}$	2.95	0.62	3.57
$\text{WO}_3\text{-NWH-NaCl}$	2.69	0.75	3.44
$\text{WO}_3\text{-NWH-NaBr}$	2.84	0.67	3.51
$\text{WO}_3\text{-NWH-NaI}$	2.78	0.70	3.48
$\text{WO}_3\text{-NWH-KCl}$	2.64	0.77	3.41
$\text{WO}_3\text{-NWH-KBr}$	2.66	0.76	3.42
$\text{WO}_3\text{-NWH-KI}$	2.54	0.82	3.36
$\text{WO}_3\text{-AMT-HF}$	2.94	0.62	3.56
$\text{WO}_3\text{-AMT-HCl}$	2.25	0.97	3.22
$\text{WO}_3\text{-AMT-HBr}$	2.53	0.83	3.36
$\text{WO}_3\text{-AMT-HI}$	2.77	0.71	3.48

2.3. Crystal Phase and Crystallite Mean Size Determination

X-ray diffraction (XRD) patterns were recorded to investigate the crystal phase and crystal phase composition of the WO_3 and $\text{WO}_3 \cdot 0.33\text{H}_2\text{O}$ materials. In the NWH-NaX/KX series case, the $\text{WO}_3 \cdot 0.33\text{H}_2\text{O}$ partial hydrate was identified in all samples (JCPDS file no. 35-1001) [55]. The differences in the XRD patterns of the NWH-NaX and NWH-KX (Figure 3) could be explained by assuming that the K^+ cation has a negative effect while Na^+ has a positive effect on the crystallinity of the WO_3 . Additionally, the Na^+ and K^+ ions' impact can be linked with the samples' particle size as well (10–40 nm for NaX series; ≈ 10 nm for the KX series). In the NaX series, the average crystallite size decreases from 36.7 nm to 14.1 nm, while, in the case of the KX series, it increases from 8.7 (KCl) to 10.8 nm (KI). Another cause of the difference could be that the NWH-KX series samples are built up from smaller crystals forming large aggregates. In contrast, the samples from the NWH-NaX series were built up from bundles.

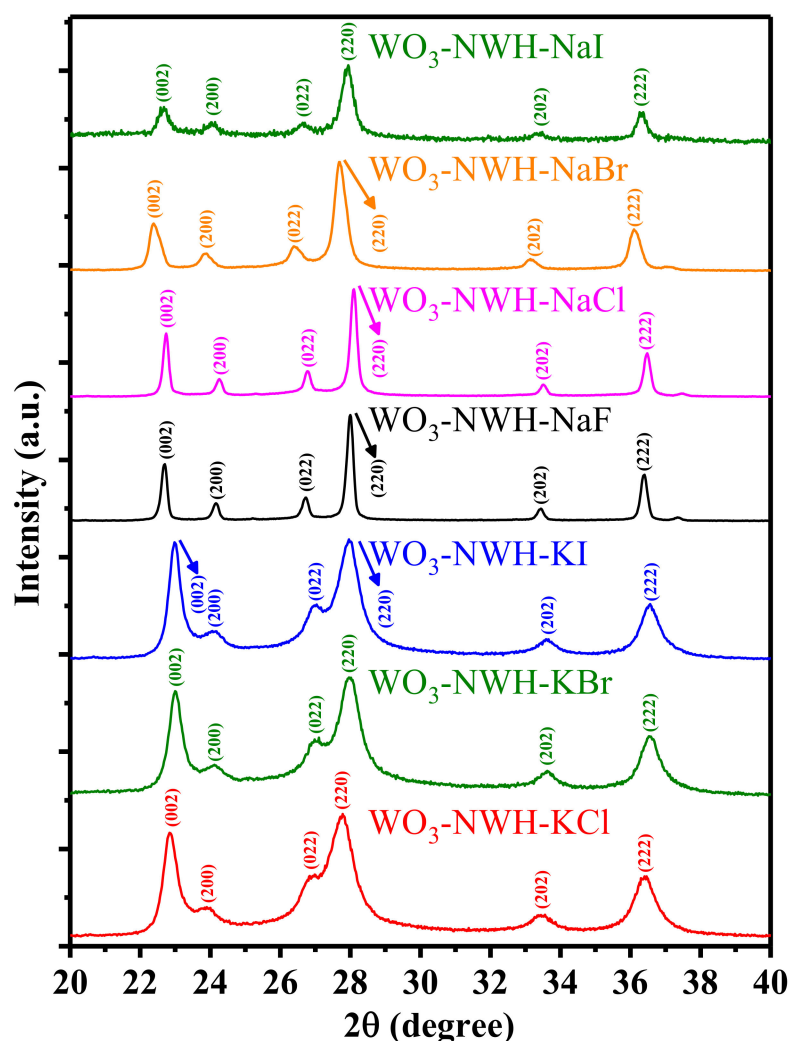


Figure 3. XRD patterns of synthesized WO_3 semiconductors from NWH-NaX and NWH-KX series.

Samples from the third series (AMT-HX) contained two crystal phases: partial hydrate and monoclinic WO_3 (Figure 4). Interestingly, the sample WO_3 -AMT-HCl contained only the monoclinic crystal phase (JCPDS file no. 43-1035) [56]; in the WO_3 -AMT-HI sample, only the partial hydrate crystal phase was present. The samples denoted as WO_3 -AMT-HF and WO_3 -AMT-HBr (Figure 5) contain both crystal phases with 87.5% partial hydrate—12.5% monoclinic and, respectively, 30.76% partial hydrate—69.23% monoclinic crystal phase distribution. The size of the aggregates in the WO_3 -AMT-HF sample was between 0.1–1 μm ; spherical crystals were observed, which were built up from smaller nanoplates of 14 nm. The stars' diameter in the WO_3 -AMT-HCl sample were between 3 and 4 μm (assembled from numerous smaller nanowires with a diameter of 10–15 nm). Similar traits were observed in the WO_3 -AMT-HBr sample, which was built from 34 nm sized nanowires. Stars were also observed in the WO_3 -AMT-HI sample (2–3 μm , from 27 nm sized nanowires).

Sodium and potassium halides and, subsequently, hydrohalic acids, might deteriorate or cause changes in the WO_3 structure because Na^+ , K^+ , and H^+ species could be adsorbed on particular facets, and might even occupy defect sites in the lattice, which ultimately can lead to crystal structure rearranging, which is linked to stoichiometric changes in tungsten trioxide [57].

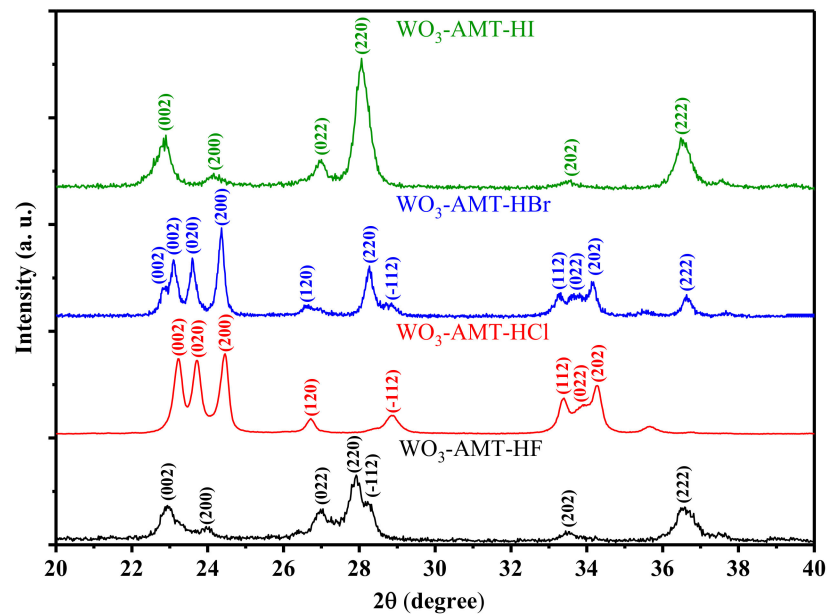


Figure 4. XRD patterns of synthesized WO_3 semiconductors from the AMT-HX series.

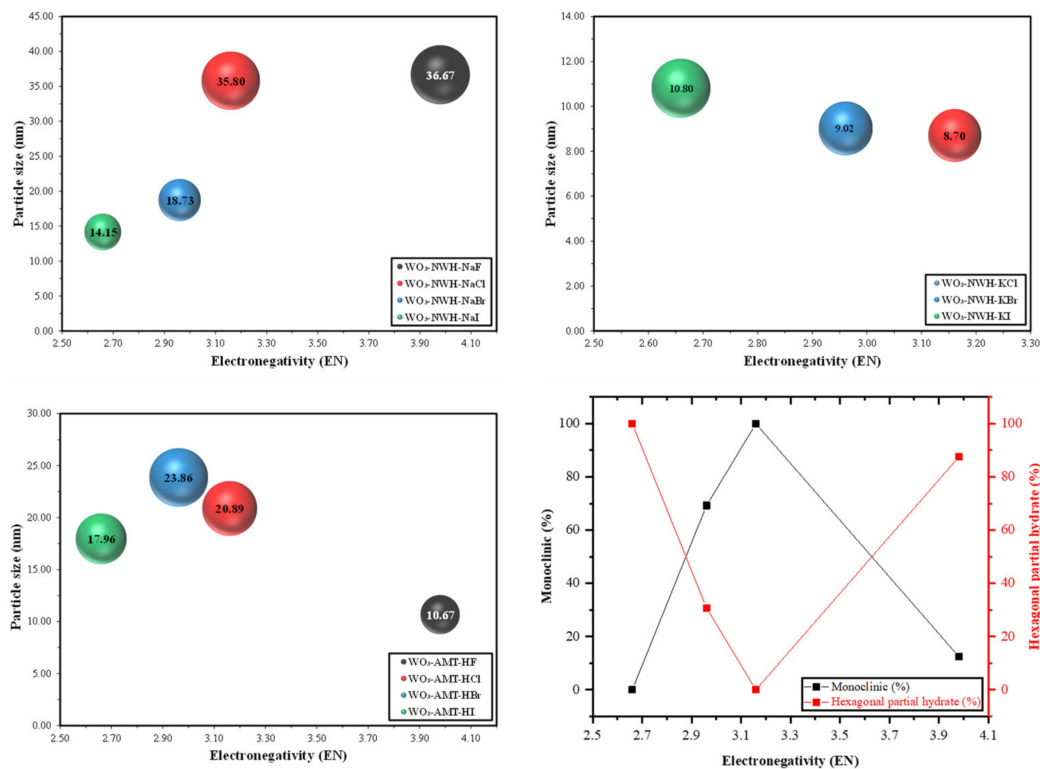


Figure 5. Distribution of the average crystallite size of the $\text{WO}_3\text{-NWH-NaX}$, KX and AMT-HX samples in the function of electronegativity and the change in the crystal phase composition for the sample series AMT-HX.

The crystallite mean size of the WO_3 materials was calculated using the Scherrer equation. By applying Bragg's law, we calculated the samples' d-spacing (Table 3). However, the obtained results by using the Scherrer equation are trustworthy only between 10–100 nm. Considering this, we calculated the crystallite mean size and lattice strain for all samples at the 28 2θ reflections. The $\text{WO}_3\text{-NWH-NaX}$ series did not display a direct link between the electronegativity of applied salt anions and the calculated lattice strain of the samples, but in the case of the $\text{WO}_3\text{-NWH-KX}$ and $\text{WO}_3\text{-AMT-HX}$ series, a direct link

can be found between electronegativity and the lattice strain, where high electronegativity lead to higher lattice strain values ($\text{WO}_3\text{-NWH-KCl}$ —0.0245; $\text{WO}_3\text{-AMT-HF}$ —0.0121); subsequently, low electronegativity lead to lower lattice strain values ($\text{WO}_3\text{-NWH-KI}$ —0.0153; $\text{WO}_3\text{-AMT-HI}$ —0.0072). This behavior can be explained by the perovskite ABO_3 crystal structure, which has an empty A site. This feature gives an open crystalline structure, which is prone to host interstitial species (in our case, cations and anions), indicating that its structure can be doped [58].

Table 3. Crystallite mean size and lattice strain of the WO_3 semiconductors.

Sample	Crystallite Mean Size (nm)	Lattice Strain
$\text{WO}_3\text{-NWH-NaF}$	34.2	0.0044
$\text{WO}_3\text{-NWH-NaCl}$	35.7	0.0042
$\text{WO}_3\text{-NWH-NaBr}$	20.4	0.0074
$\text{WO}_3\text{-NWH-NaI}$	18.2	0.0082
$\text{WO}_3\text{-NWH-KCl}$	6.1	0.0245
$\text{WO}_3\text{-NWH-KBr}$	8.4	0.0179
$\text{WO}_3\text{-NWH-KI}$	9.8	0.0153
$\text{WO}_3\text{-AMT-HF}$	12.4	0.0121
$\text{WO}_3\text{-AMT-HCl}$	17.9	0.0085
$\text{WO}_3\text{-AMT-HBr}$	32.9	0.0061
$\text{WO}_3\text{-AMT-HI}$	20.9	0.0072

2.4. Raman Spectroscopy

Raman spectroscopy can provide relevant information about the crystallinity and phase composition of the samples. It can also be employed to determine surface defects or oxygen vacancies on the material's surface, which is of particular interest, especially in heterogeneous photocatalysis.

The Raman spectra of the WO_3 SCs series are illustrated in Figure 6. The vibrational band observed at 132 cm^{-1} in all spectra was attributed to lattice vibrations of WO_3 [59]. In the case of the NaX series, the band at 257 cm^{-1} was observed, due to the bending vibrations of the O=W=O bonds, which is specific for the hydrated types of tungsten trioxide [60], while, in the case of the KX series, the band at 262 cm^{-1} can be assigned to the bending vibrations of the O-W-O bonds [61]. We found it quite interesting that the latter one was not present in the NaX series spectra. The band at 325 cm^{-1} corresponds to the vibrations of $\text{O-W}^{+5}\text{-O}$. It proves the presence of surface defects or oxygen vacancies in the samples [62].

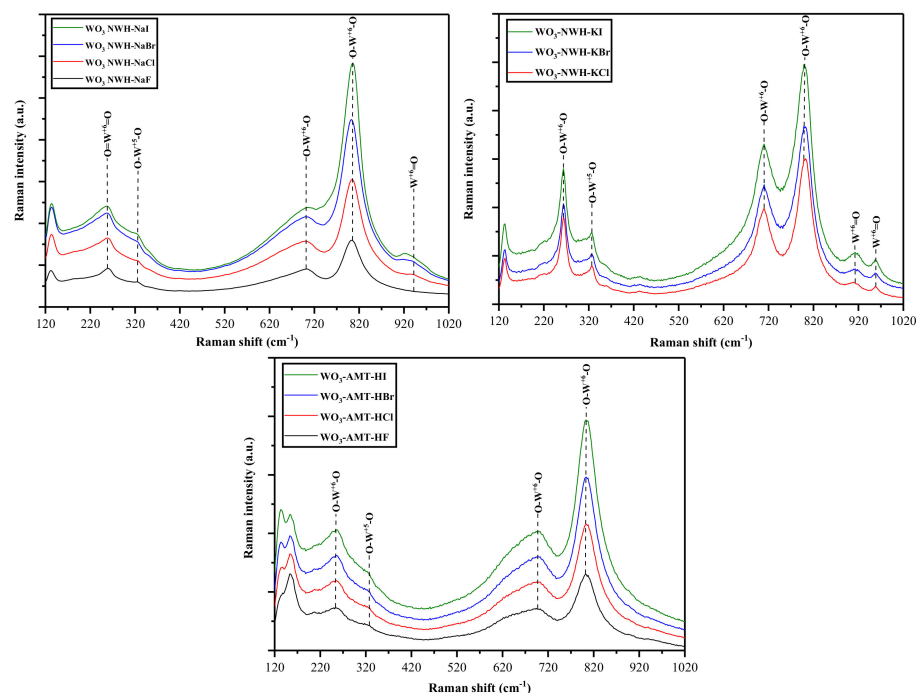


Figure 6. Raman spectra of the WO_3 -NWH-NaX, KX, and AMT-HX series.

In the Raman spectra of the NaX series, the bands at 701 and 804 cm^{-1} correspond to the bending and stretching modes of the $\text{O-W}^{+6}\text{-O}$ bonds [63,64], while, in the case of the KX series, the bands at 710 and 801 cm^{-1} are due to the O-W-O bending and stretching vibration modes [64,65]. Moreover, the band at 944 cm^{-1} observed in the spectra of the NaX series was attributed to the vibrational modes of $\text{W}^{+6}=\text{O}$, which is also specific for the hydrated types of tungsten trioxide [64]; similarly, the bands from 914 and 954 cm^{-1} evidenced in the spectra of KX series were assigned to the $\text{W}^{+6}=\text{O}$ (terminal) bond vibrations [66,67].

The Raman spectra of the two series of WO_3 materials were compared. A significant difference was observed: the KX series bands were more intense and sharper than those of the NaX series. The XRD patterns and Raman spectra of the NaX series lead to the conclusion that the samples' crystal phase is hexagonal partial hydrate ($\text{WO}_3 \cdot 0.33\text{H}_2\text{O}$), and also that, as the electronegativity of the added ions diminishes, so does the crystallinity of the materials.

The XRD patterns of the KX series concluded (Section 2.3) that the samples' crystallinity is relatively low compared to the NaX series, possibly caused by the intercalation of the K^+ ions in the system. However, the Raman spectra would suggest a high crystallinity rate by observing the bands at 262 , 327 , 710 , and 801 cm^{-1} . The presence of these bands, their intensity, and their sharpness would suggest the monoclinic crystal phase, but the $\text{W}^{+6}=\text{O}$ bond vibrations were also identified in the KX series samples spectra, which proves the presence of hydrated tungsten trioxides. One explanation for this could be that, in these samples, there are two crystal phases: monoclinic and $\text{WO}_3 \cdot 0.33\text{H}_2\text{O}$, but the latter is more abundant, whereas the monoclinic WO_3 is present in low quantities, and therefore the low crystallinity is observed in the XRD patterns. Another explanation could be that we have amorphous tungsten trioxide in our samples, which can be linked to the XRD patterns of the KX series (Figure 3).

In the Raman spectra of the WO_3 -AMT-HX series (Figure 6), the lattice vibrations of WO_3 were identified at 133 and 155 cm^{-1} [68,69], the W-O-W bending mode at 252 cm^{-1} [70], the $\text{O-W}^{+5}\text{-O}$ vibrations at 327 cm^{-1} [64], and the $\text{O-W}^{+5}\text{-O}$ stretching modes at 697 and 804 cm^{-1} [71,72]. Thus, the Raman spectra of the HX series would suggest the monoclinic crystal phase for every semiconductor in the series. Simultaneously, in the $900\text{--}1000\text{ cm}^{-1}$ range, no band was identified—this interval is specific for $\text{W}^{+6}=\text{O}$ bonds and is strongly correlated with hydrated types of WO_3 . By comparing the XRD pattern of the HX series

(Figure 6) with the Raman spectra (Figure 7), it is evident that, in this case, there are also two crystal phases present in the samples, except for $\text{WO}_3\text{-AMT-HCl}$ (monoclinic) and $\text{WO}_3\text{-AMT-HI}$ (hexagonal partial hydrate).

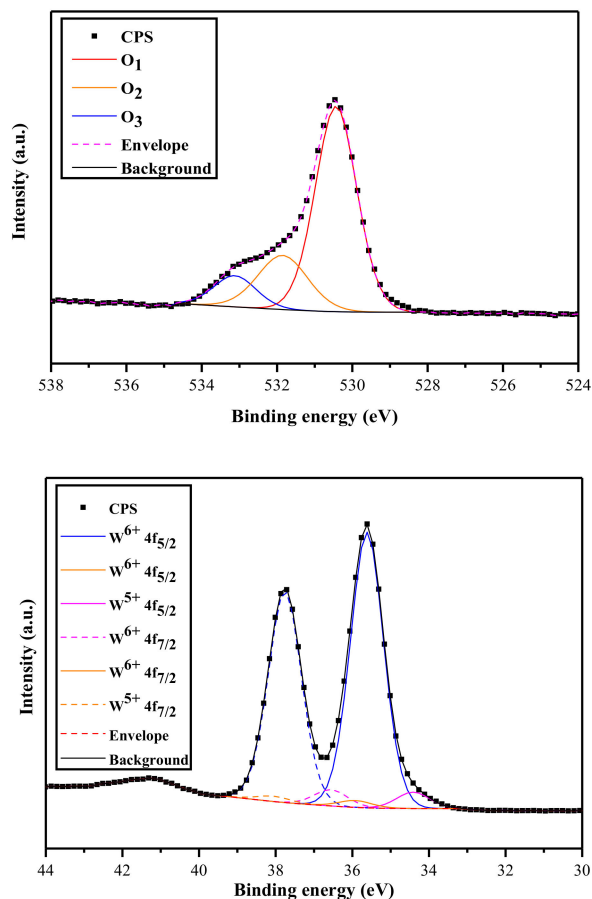


Figure 7. XPS spectra of $\text{WO}_3\text{-AMT-HF}$ sample—O1s deconvolution (top), W4f deconvolution (bottom).

Thus, the Raman spectra analysis revealed that, in the first two SCs series ($\text{WO}_3\text{-NWH-NaX}$ and $\text{WO}_3\text{-NWH-KX}$), bands specific to hydrated tungsten oxides were present. Still, in the latter, the peaks were more intense. Another band in the $900\text{--}1000\text{ cm}^{-1}$ region related to $\text{W}^{+6}=\text{O}$ was noticed, which could be explained by the presence of $\text{WO}_3\cdot\text{H}_2\text{O}$ and not hexagonal partial hydrate ($\text{WO}_3\cdot 0.33\text{H}_2\text{O}$).

The observed Raman bands in the third series ($\text{WO}_3\text{-AMT-HX}$) spectra would suggest a monoclinic crystal phase for each sample. Still, unusual behavior can be seen concerning the lattice vibrations (bands below 200 cm^{-1}); more precisely, the intensity of the bands at 133 and 155 cm^{-1} changes, and also the ratio of the bands changes as the electronegativity decreases, which means that the exposed crystallographic planes of WO_3 are affected by the presence of anions and cations, leading to changes in the crystal structure.

Although there are no bands that would indicate the presence of the partial hydrate crystal phase, the lattice vibration changes suggest that the adsorbed water amount on the materials' surface diminishes as the electronegativity decreases and might even influence how the crystals are built up, more likely leading to $\text{WO}_3\text{-}\delta$ and not $\text{WO}_3\text{-}\gamma$ (monoclinic), meaning that the WO_3 is not built up by the well-known two WO_3 octahedra junction. This not-so-common junction impacts the SCs structure, stoichiometry, band gap value, and particle size, and ultimately their photocatalytic and electrochromic activity [73].

2.5. X-ray Photoelectron Spectroscopy

For each sample of the three series, the surface chemical composition was studied by XPS core level analysis. As a result, the elemental composition for a particular samples'

series was comparable, but differences were found among the three series. For example, besides the expected W, O, and C elements, the survey spectra disclosed K^+ in the WO_3 -NWH-KX samples (8%), Na^+ in the WO_3 -NWH-NaX samples (3%), and a relatively increased C amount in the WO_3 -AMT-HX samples.

Each sample presented three components in the W4f signal in different proportions, depending on the crystal phase. W^{6+} states of oxide, hydroxide, and W^{5+} states were identified, centered at 35.65, 36.05, and 34.45 eV (± 0.05 eV), where $W4f^{5/2}$ was presenting 2.1 eV spin-orbit splitting of $W4f^{7/2}$ [74]. Only subtle changes occur in the distribution of W4f components in the WO_3 -NWH-NaX and WO_3 -NWH-KX samples. Essential differences were observed in WO_3 -AMT-HCl and WO_3 -AMT-Br, where the (W^{6+} —OH) component increased (WO_3 -AMT-HF: 2.3%, WO_3 -AMT-HCl: 34.7%, WO_3 -AMT-HBr: 22.5%, WO_3 -AMT-HI: 8.6%). However, these two samples exhibit a dominantly monoclinic crystal phase.

The other samples with the hexagonal phase presented the (W^{6+} —OH) component under 10% of the total W amount. On the other hand, W^{5+} species were present in a meager amount, under 5% (except the sample WO_3 -AMT-HF, showing ~6% of W^{5+}). In comparison, the sample AMT-HCl was monoclinic and showed only 2.6% of W^{5+} .

Even though there are samples from both WO_3 -NWH-KX and WO_3 -NWH-NaX series with a higher percentage of W^{5+} than the sample WO_3 -AMT-HCl, inhibition was observed on the photocatalytic conversion values. Hence, WO_3 samples in composite systems could inhibit the photoactive semiconductor performance independently from the W^{5+} amount, meaning that surface defects can affect photocatalytic performance [75,76]. However, the highest activity was shown in sample WO_3 -AMT-HF (Figure 7), with the highest W^{5+} concentration.

Three different O species were identified in the O1s spectra of the samples at 530.5, 531.9, and 533.2 eV, which were identified as follows: the crystal lattice oxygen " O_1 " [77], the adsorbed oxygen species from the surface [78], the oxygen-deficient regions of WO_3 " O_2 ", and subsequently, the adsorbed water molecules on the surface of WO_3 " O_3 " [79]. The signal located at 531.9 eV was not investigated in detail. Likewise, it contains the W-OH, C=O, and C-OH surface groups, with insignificant peak location differences, making the fitting process unreliable. In the WO_3 -NWH-KX and WO_3 -NWH-NaX samples, surface water is under 5% of the total O amount. In contrast, in the WO_3 -AMT-HX samples, the water amount in the HF sample, starting with approximately 10%, decreases with the anion's electronegativity. However, they do not share the same crystal phase.

Samples WO_3 -AMT-HF, with a hexagonal crystal phase, and WO_3 -AMT-HCl, with monoclinic crystal phase—with a high percentage of adsorbed water (~8–10%)—facilitated the photocatalytic activity of TiO_2 in composite systems, while WO_3 -AMT-HB, with a mixed-phase, and WO_3 -AMT-HI, with a hexagonal crystal phase—with lower adsorbed water amount (<5%)—inhibited the TiO_2 photocatalytic activity, pointing out possible importance of the surface hydrophilicity.

Furthermore, inhibition occurs in composite systems, employing WO_3 -NWH-KX and WO_3 -NWH-NaX samples with the hexagonal phase, which could be attributed to the low adsorption affinity (the amount of adsorbed water was <5%, as in AMT-HBr and AMT-HI samples). Different anions did not cause any consistent modification of W's and O's surface states; the varied amount of water did not systematically affect the TiO_2 photocatalytic performance.

2.6. Photocatalytic Activity and Kinetic Study

After two hours, a 6.5% adsorption of the MO was observed; subsequently, photolysis induced a 2.1% degradation rate of the chosen model pollutant (Figure 8). Commercial P25 yielded an 82.8% conversion of the dye under UV light irradiation, whereas the kinetic study proved a fractional reaction order ($n = 0.5$): 0.0542 at an apparent rate constant ($\mu M^{0.5} \cdot s$)⁻¹. For each "bare" WO_3 SC from all series, photocatalytic tests were carried out. However, they did not show any photocatalytic activity nor adsorption of the MO. The

photocatalytic efficiency of the composites, and subsequently of the commercial TiO_2 (P25), was determined by applying the following equation:

$$X = [1 - (C_f/C_i)] \times 100$$

where X is the conversion rate given in percentage, C_f is the solution concentration after 2 h of ultraviolet irradiation, and C_i is the initial concentration. Concerning the kinetics (for all composites systems) of methyl orange aqueous solution degradation, we determined the apparent rate constants (k_{app}) by plotting the concentration against the irradiation time. The slope was attributed as the rate apparent constant. Regarding the P25 methyl orange degradation kinetics, we calculated the apparent rate constant by plotting the $C^{0.5}$ against the irradiation time. The slope corresponds to the apparent rate constant.

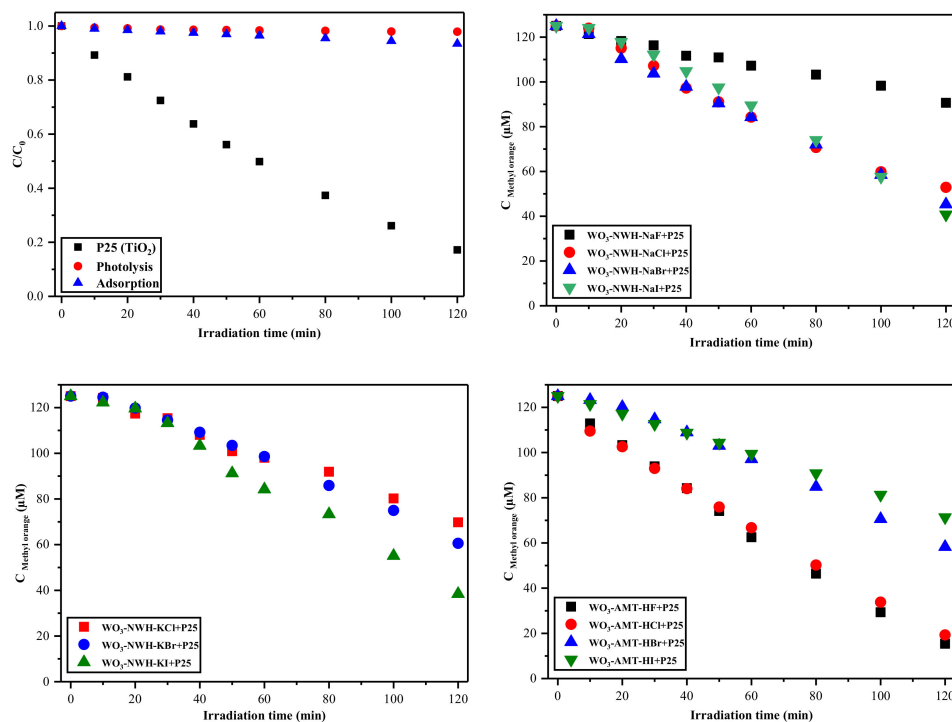


Figure 8. Adsorption on the P25 surface, photolysis, and degradation with all the composites under UV light irradiation.

Figure 8 and, furthermore, Table 4 present the effect of electronegativity upon the composite materials' photocatalytic efficiency. In both the $\text{WO}_3\text{-NWH-NaX}$ and $\text{WO}_3\text{-NWH-KX}$ series, the low electronegativity of the applied salt during synthesis had a beneficial impact on the photoactivity (increased the activity from 27.5% → 67.4% and 44.2% → 69.3%). However, a lower performance was obtained compared to commercial P25 (82.8%). The kinetics was a zeroth-order reaction and followed the trend of the conversion values. An interesting trend was observed concerning the photocatalytic efficiency of the third series (Figure 8 and Table 4) $\text{WO}_3\text{-AMT-HX}$: increased electronegativity of the added hydrohalic acids led to higher conversion rates. Only samples from this series prepared composite systems exhibited higher photocatalytic activity ($\text{WO}_3\text{-AMT-HF}$ —87.7%; $\text{WO}_3\text{-AMT-HCl}$ —84.6%) than the reference photocatalyst (commercial P25—82.8%). Regarding the MO degradation kinetics with $\text{WO}_3\text{-AMT-HX+P25}$ composite systems, a zeroth-order reaction was established as before, which is in a good argument with the obtained R^2 values.

Table 4. Kinetics of methyl orange degradation under UV light irradiation with WO₃-P25 composites.

Sample	Reaction Order (<i>n</i>)	Rate Apparent Constant (k_{app}) ($\mu\text{M}\cdot\text{min}^{-1}$)	R ²	Conversion (X) (%)
WO ₃ -NWH-NaF+P25	0	0.2713	0.993	27.5
WO ₃ -NWH-NaCl+P25		0.6514	0.986	57.7
WO ₃ -NWH-NaBr+P25		0.6675	0.998	63.7
WO ₃ -NWH-NaI+P25		0.7297	0.990	67.4
WO ₃ -NWH-KCl+P25		0.4697	0.991	44.2
WO ₃ -NWH-KBr+P25		0.5526	0.990	51.5
WO ₃ -NWH-KI+P25		0.7534	0.988	69.3
WO ₃ -AMT-HF+P25		0.9195	0.996	87.7
WO ₃ -AMT-HCl+P25		0.8603	0.996	84.6
WO ₃ -AMT-HBr+P25		0.5856	0.989	53.4
WO ₃ -AMT-HI+P25		0.4477	0.999	42.9
Sample		Reaction Order (<i>n</i>)	Rate Apparent Constant (k_{app}) ($\mu\text{M}^{0.5}\cdot\text{s}^{-1}$)	R ²
P25	0.5	0.0542	0.999	82.8%

3. Correlations between Structural and Optical Parameters between Structural, Optical, Electronegativity, and the Assessed Photocatalytic Performance

Although in the WO₃-NWH-NaX and WO₃-NWH-KX series, electronegativity did not systematically affect either the W⁵⁺, W⁶⁺ species or the samples' band gap value, they still influence each other (Figure 9). In the case of the WO₃-NWH-NaX series, we observed that a higher amount of W⁵⁺ species (4.10 and 4.06%) shifts the band gap value towards the visible region (2.78 and 2.69 eV); subsequently, a lower amount (3.07 and 2.70%) will shift the band gap value towards the UV region (2.95 and 2.84 eV). We observed similar behavior for the WO₃-NWH-KX series (Figure 9), but here, W⁶⁺ species had influenced the samples' band gap value. Although the band gap of every sample is in the visible region, a higher amount of W⁶⁺ species (36.3 and 34.4%) caused a redshift (2.54 and 2.64 eV). In contrast, the lower amount of W⁶⁺ (32.2%) led to a slight blue shift (2.66 eV).

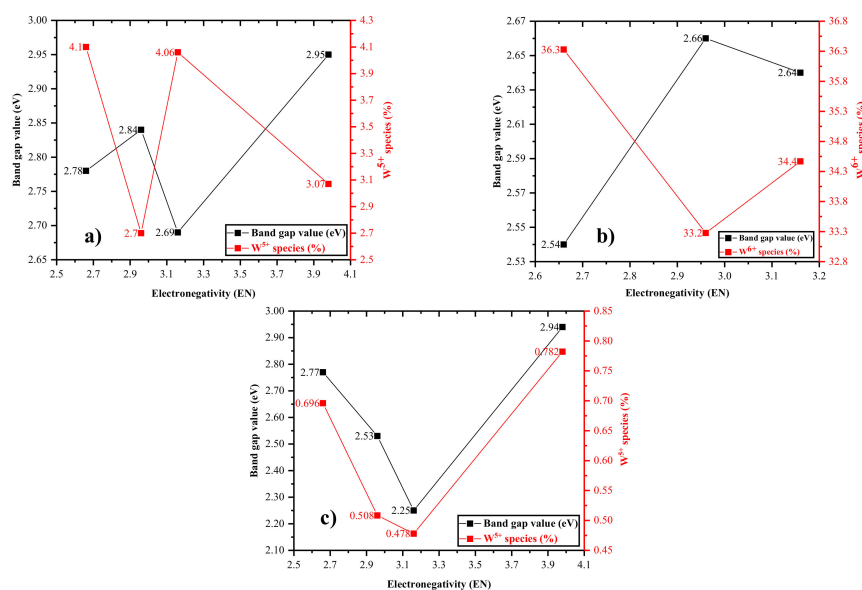


Figure 9. Correlations established between W⁵⁺ and W⁶⁺ species (XPS), and the band gap value: WO₃-NWH-NaX series (a); WO₃-NWH-KX series (b); WO₃-AMT-HX series (c).

In the third series (WO₃-AMT-HX), a different behavior was observed (Figure 9) than in the first two series; namely, that a high amount of W⁵⁺ species (0.78 and 0.70%) shifted the band gap to the UV region (2.94 and 2.77 eV). In contrast, a lower amount of W⁵⁺ (0.51 and 0.48%) moved the band gap energy values toward the visible region (2.53 and 2.25 eV). This behavior is very unusual because W⁵⁺ is an indicator of the blue color, and it should result in absorbance towards the red color region. In the third series, the amount of W⁵⁺ species directly affected the band gap of the samples (Figure 10).

Regarding the HX series, exciting correlations were found between the XRD and DRS data (Figure 10, top). Although, on first impression, no discernible link seems to exist, we found that if the respective anions' electronegativity (EN) was extremely low, and subsequently high, the particle size was the smallest; subsequently, if the EN was around three or close to it, then the average particle size was the highest. The same behavior was observed for the band gap energy values of the samples; broader band gap values were determined for the SCs obtained in the presence of the highest and lowest anion EN (2.94 eV for the WO₃-AMT-HF samples and 2.77 eV for the WO₃-AMT-HI samples), and the smallest for materials with EN ≈ 3 (2.25 eV for WO₃-AMT-HCl and 2.53 eV for WO₃-AMT-HBr). Furthermore, it was observed that the crystal phase composition could also be linked to the band gap values of the SC materials (Figure 10, bottom); more precisely, the presence of the hexagonal partial hydrate (HPH) crystal phase led to broader band gaps; when HPH was 100%, the band gap of the sample was 2.77 eV; HPH 87.5%—2.94 eV; HPH 30.76%—2.53 eV; subsequently, when HPH was 0% (not present) the band gap was 2.25 eV.

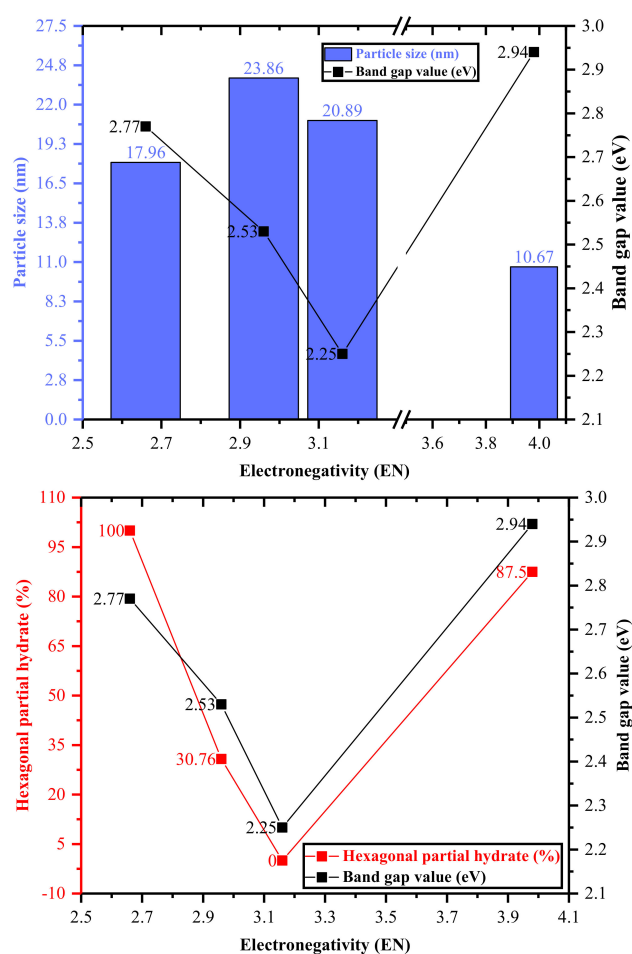


Figure 10. Correlations established for the WO₃-AMT-HX series between particle size and band gap value (top), respectively hexagonal partial hydrate percentage and the band gap value (bottom).

The band gap values of the WO_3 -AMT-HF+P25 and WO_3 -AMT-HCl+P25 composites were 3.10 and 3.01 eV, meaning that they are photoactive under UV light irradiation; these samples yielded the highest photocatalytic performance, thus proving that the monoclinic crystal phase was beneficial for MO degradation, but also that there should be a well-defined balance between the hexagonal partial hydrate (HPH) and the monoclinic crystal (MC) phase's presence in the material. The optimum ratio seems to be around 87.5:12.5 (HPH to MC), which is very close to the 89:11 anatase rutile ratio in TiO_2 . In our previous work [80], a similar phenomenon was observed. We obtained WO_3 from tungstic acid, which lead to a semiconductor with a 90.6:9.3 (HPH to MC) crystal phase ratio. In a composite system with TiO_2 (P25+ WO_3 -HW, band gap was 3.00 eV, conversion rate 87.2%), a higher conversion rate was achieved for phenol removal than with bare TiO_2 .

The presence, or even more importantly, the absence, of the water band in the XPS spectrum could be evidence of oxygen vacancies on the materials' surface. These vacancies are significant in heterogeneous photocatalysis. Figure 11 (top) proves that EN influences the anchored water molecules' presence upon the SCs' surface, directly affecting the composite systems' photocatalytic efficiency; as the EN of the halide anion diminishes (and as the pK_a of the hydrohalic acids strengthens), the amount of anchored water on the surface decreases, which leads to structural defects and oxygen vacancies. Figure 11 (bottom) also provides information on how the water band and the lattice vibrations are linked. We observed that the ratio of the I_{133}/I_{155} lattice vibrations increased as the pK_a of the hydrohalic acids grew stronger. It also affected the water band because the water band percentage diminished as the lattice vibrations ratio amplified. By adding different hydrohalic acids to the synthesis solution, the incorporation of H^+ into the WO_3 crystal structure may be possible, which was evidenced by the changes in the lattice vibrations (133 and 155 cm^{-1}) and, subsequently, in the water band in the XPS spectra (Figure 11), which lead to surface defects and oxygen vacancies. However, this resulted in the formation of recombination centers for photogenerated charge carriers; the photoactivity followed a decreasing trend as the acid H^+ concentration grew [81,82].

The presence of surface defects (Figure 12) was assessed from the ratio of the I_{327}/I_{701} , I_{327}/I_{804} , and, subsequently, the I_{327}/I_{802} cm^{-1} bands, which were chosen because the band at 327 cm^{-1} gives information about the W^{5+} presence, the band at 701 cm^{-1} provides information about W^{+6} , and the one at 802 cm^{-1} provides information about the lattice vibrations in the WO_3 structure. We observed an interesting trend between the MO degradation and the WO_3 materials' surface defects, which, at first sight, might be surprising. Still, the surface defects have a negative impact on the photocatalytic activity of the composite systems. This negative impact could be strongly related to the fact that surface defects facilitate the generation of $\bullet\text{OH}$, not the charge separation of electrons and hole pairs (e^- , h^+). The kinetics of the MO degradation, which, for all TiO_2/WO_3 composites, was zeroth order, lead to the conclusion that MO degradation occurred by direct hole oxidation during the photocatalytic tests and not with radicals. Similar behavior was observed in our previous work and by others also [83,84]. Still, another explanation could be that we followed the dye's degradation with a UV-Vis spectrophotometer, which gives information about the dye's decolorization. The MO's color is related to the $-\text{N}=\text{N}-$ bonds in its structure, and these bonds are directly decomposed with holes (h^+).

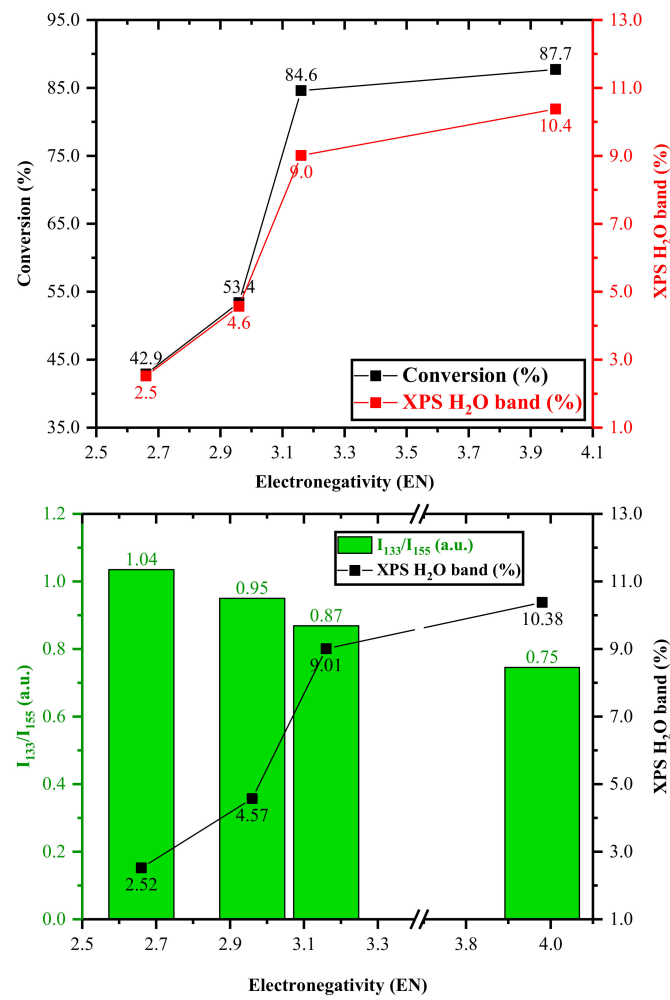


Figure 11. Correlations established for the WO₃-AMT-HX series between conversion and water band percentage (top) and lattice vibrations' ratio and water band percentage (bottom).

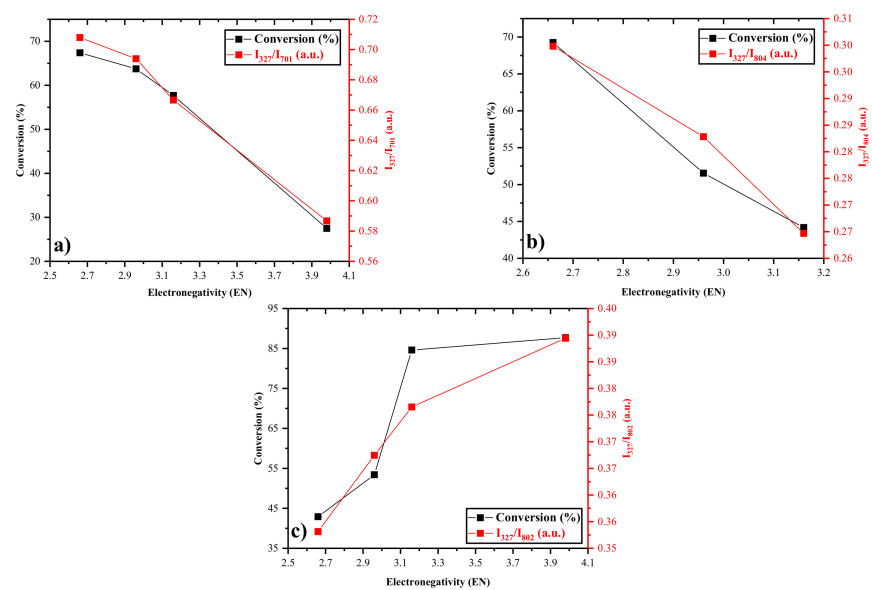


Figure 12. Correlations between photocatalytic efficiency and surface defects: WO₃-NWH-NaX series (a); WO₃-NWH-KX series (b); WO₃-AMT-HX series (c).

The electronegativity of the used halide salts and hydrohalic acids in the synthesis influenced the presence of surface defects as follows: in the case of the first two series, the higher electronegativity of the used anion led to a higher amount of surface defects, but in the case of the third series, the increased acidity (pK_a) of the acids leads to a higher amount of surface defects. Even if other parameters influenced the quantity of surface defects, the same behavior was observed in all three samples: a higher ratio of surface defects leads to higher photocatalytic activity.

This study proves that the electronegativity of the anions used during the synthesis has a crucial role in the morphology, crystal structure, and crystal phase composition of the SCs, which influence the samples' photocatalytic activity. Still, it is essential to mention that, just as significant (or probably even more significant), are the precursors, synthesis route, or composite preparation methods of the materials. Thus, this study only partially answers the impact of electronegativity on TiO_2/WO_3 composite systems' photocatalytic activity. More similar studies should follow to discuss the electronegativity effect upon the WO_3 SCs obtained from other precursors or synthesis methods.

4. Materials and Methods

4.1. Chemicals

Sodium tungstate dihydrate ($Na_2WO_4 \cdot 2H_2O$, Sigma–Aldrich, St. Louis, MI, USA, 99.9%), ammonium metatungstate hydrate (AMT) ($(NH_4)_6H_2W_{12}O_{40} \cdot xH_2O$, Sigma–Aldrich, 99.9%), hydrogen peroxide (H_2O_2 , Sigma–Aldrich, 30%), hydrochloric acid (HCl, CHEM, Chemical Company, Iași, Romania, 35–38%, 12 M), sodium chloride (NaCl, CHEM, 99.5%), sodium fluoride (NaF, Fluka AG, Buchs, Switzerland, 99%), sodium bromide (NaBr, Alfa Aesar, Haverhill, MA, USA, 99%), sodium iodide (NaI, Reanal, 99.99%), potassium fluoride dihydrate ($KF \cdot 2H_2O$, CHEM, 99.5%), potassium chloride (KCl, CHEM, 99%), potassium bromide (KBr, Reanal, 99.99%), potassium iodide (KI, VWR Chemicals, Radnor, PA, USA, 99.99%), hydrofluoric acid (HF, Merck, Alexandria, VA, USA, 48%), hydrochloric acid (HCl, CHEM, 35–38%), hydrobromic acid (HBr, Alfa Aesar, 47–79%), and hydroiodic acid (HI, Merck, 57%) were used as received. In addition, 125 μ M aqueous solution of methyl orange (MO) ($C_{14}H_{14}N_3NaO_3S$, CHEM, 85%) was used to determine the photocatalytic activity.

4.2. Synthesis of WO_3 and $WO_3 \cdot 0.33H_2O$ Semiconductors

In the first series, 3.29 g of $Na_2WO_4 \cdot 2H_2O$ and 0.83 g of NaF (NaCl—1.16 g; NaBr—2.04 g; NaI—2.97 g) was dissolved in 75 mL distilled water under constant stirring. The solutions' pH was adjusted to 2 with a 3 M HCl (12 M) aqueous solution and was stirred for 24 h at room temperature.

The second series was made following the same procedure by using 0.93 g of $KF \cdot 2H_2O$ (1.48 g of KCl; 2.36 g of KBr; 3.29 g of KI). The solutions were hydrothermally heat-treated at 180 °C for 24 h, and a precipitate was finally obtained, which was collected and washed by centrifugation, for 3×10 min at 6000 rpm, with distilled water. Afterward, the products were dried at 80 °C for 12 h and were coded as follows: WO_3 -NWH-NaX and WO_3 -NWH-KX. The NWH abbreviation originates from the sodium tungstate dihydrate's molecular formula $Na_2WO_4 \cdot 2H_2O$, and the X stands for the halide anions (F^- , Cl^- , Br^- , and I^-). It should be noted that when KF was applied (several experiments were carried out), WO_3 did not crystallize. The reason for this could be that F^- anions hindered the precipitation of WO_3 .

In the third series, 1.23 g AMT and 0.46 mL HF (49%) (subsequently, 0.84 mL of HCl (37%); 1.43 mL of HBr (47–79%); 1.19 mL of HI (99.99%)) were dissolved in 12.5 mL of distilled water. The solutions were stirred for 15 min, then hydrothermally treated at 180 °C for 4 h, and colloidal suspensions were obtained. The suspensions were collected and washed by centrifugation at 6000 rpm for 3×10 min with distilled water. After centrifugation, the precipitates were dried for 6 h at 70 °C. Finally, the as-obtained WO_3 nanostructures were annealed in air at 500 °C for 30 min. The obtained catalysts were named WO_3 -AMT-HX.

The AMT abbreviation originates from the ammonium metatungstate hydrate compounds' names, and X denotes the hydrohalic acid's anions.

4.3. Preparation of WO_3 - TiO_2 Semiconductor Nanocomposites

In each case, a specific ratio was established between the composite components, according to our previous work: 24% WO_3 and 76% TiO_2 (Evonik Aeroxide P25) [85–87]. The nanocomposites were obtained via mechanical mixing in an agate mortar for 3×5 min [85,88]. They were named WO_3 according to the precursor name and corresponding halide salt or hydrohalic acid + P25. The Evonik Aeroxide TiO_2 will be mentioned as P25 later on.

4.4. Methods and Instrumentation, Kinetic Study and Assessment of Photocatalytic Activity

SEM micrographs were acquired using an FEI Quanta 3D FEG Scanning Electron Microscope, operating at an accelerating voltage of 25 kV.

The X-ray diffraction (XRD) investigations were conducted on a Rigaku Mini-flex-II Diffractometer using a characteristic X-ray source (CuK_{α} , $\lambda = 0.15418$ nm). The crystal phases of the WO_3 nanomaterials were identified using a PDF diffraction database using the Scherrer equation, and the average crystallite size was calculated [89].

A JASCO-V650 spectrophotometer (Jasco Inc., Easton, MD, USA) with an integration sphere (ILV-724) (Jasco Inc., Easton, MD, USA) was employed for measuring the DRS (Diffuse Reflectance Spectroscopy) spectra of the samples ($\lambda = 250$ – 800 nm). From the reflectance spectra, the light absorbance threshold for all the samples was determined and, subsequently, the band gap energy values were estimated with the help of the Kubelka–Munk equation/Tauc Plot [90].

Raman spectra were recorded with a multilaser confocal Renishaw inVia Reflex Raman spectrometer equipped with a RenCam CCD detector. As an excitation source, the 532 nm laser was applied, and the Raman spectra were collected using a 0.9 NA objective of $100\times$ magnification. The integration times were 10 s, 1800 lines/mm grating for all spectra, and 10% of the maximum laser intensity; laser power was 20 mW. The spectral resolution was about 4 cm^{-1} . In order to determine the possible presence of surface defects, the ratios of different Raman peaks were calculated: I_{327}/I_{701} (WO_3 -NWH-NaX), I_{327}/I_{804} (WO_3 -NWH-KX), and I_{327}/I_{802} (WO_3 -AMT-HX).

The X-ray photoelectron spectroscopy (XPS) spectra were recorded with a Specs Phoibos 150 MCD system equipped with a monochromatic $Al-K_{\alpha}$ source (1486.6 eV) at 14 kV and 20 mA, a hemispherical analyzer, and a charge neutralization device. The catalyst samples were fixed on a double-sided carbon tape, where the powder completely covered the tape. The binding energy scale was charged, referenced to the C1s at 284.6 eV. High-resolution W4f and O1s spectra were obtained by using an analyzer to pass energy of 20 eV in steps of 0.05 eV for the analyzed samples. The data analysis was carried out with CasaXPS software.

Concerning the photocatalytic tests, the MO dye concentration was investigated with an Analytic Jena Specord 250 plus spectrophotometer at 513 nm. The photocatalytic tests were performed under UV light irradiation in a photoreactor ($1\text{ g}\cdot\text{L}^{-1}$ suspension concentration, continuous airflow, continuous stirring, 6×6 W UV fluorescent lamps, $\lambda_{\text{max.}} = 365$ nm at a constant temperature— $25\text{ }^{\circ}\text{C}$). The suspension containing the photocatalyst and the pollutant (initial concentration of MO $C_{0, \text{MO}} = 125\text{ }\mu\text{M}$; catalyst concentration $C_{\text{photocatalyst}} = 1\text{ g}\cdot\text{L}^{-1}$; total volume of the suspension $V_{\text{suspension}} = 120\text{ mL}$) was continuously purged with air, assuring a continuous dissolved oxygen concentration during the whole experiment. The reaction rates were assessed by plotting the concentration vs. time. Zeroth order kinetics were established for each composite system regarding MO degradation.

5. Conclusions

In this study, it was found that the electronegativity of the used salts' anions impacts the photocatalytic activity of the composite semiconductors alongside the materials' morphology and structure.

Three sample series were synthesized from two precursors by adding sodium/potassium salts or hydrohalic acids to the system being studied. The series had different morphologies, and it changed with the addition of the above-mentioned compounds. The sodium halide series presented rod and wire-like morphologies—the wires formed bundles, potassium halide series also presented wire-like morphology. The hydrohalic acid series exhibited sheet/plate-like and star-like morphology. The hexagonal partial hydrate (HPH) crystal phase was observed in the samples from the sodium and potassium halides series. At the same time, the crystallinity decreased for the potassium halides samples. The average crystal size for the first series decreased with electronegativity. However, in the case of the second series, the opposite behavior was observed. Monoclinic (MC) and hexagonal partial hydrate (HPH) crystal phases were present in the hydrohalic acid-based samples: samples with HCl and HBr acids had 100% or 69% MC phase, and those with HF had a 100% MC phase. Those with HI had an 87.5% HPH crystal phase, samples that also presented the smallest average particle size.

Concerning the composite systems' photocatalytic activity, a zeroth-order reaction was established in each case, meaning that the MO mineralization mechanism occurs by direct-hole oxidation and not by $\bullet\text{OH}$ degradation; subsequently, no adsorption occurs on the surface of the composites. In the first two series, lower electronegativity yielded higher conversion rates—conversion increased as electronegativity decreased—but for the third series, this trend was quite the opposite—higher electronegativity yielded higher conversion rates (conversion decreased with electronegativity). Two composite samples had higher photocatalytic efficiency than P25. These samples ($\text{WO}_3\text{-AMT-HF+P25}$ and $\text{WO}_3\text{-AMT+HCl+P25}$) presented the highest water percentage in the XPS spectra (10.4% in $\text{WO}_3\text{-AMT-HF}$ and 9.0% in $\text{WO}_3\text{-AMT-HCl}$). Improved hydrophilicity means higher efficiency in mass transfer between the semiconductor particle and the surrounding water, resulting in improved photocatalytic efficiency. The presence of the water band in the samples is significant because a high amount will lead to lesser surface defects. In contrast, a low amount of water will lead to an abundance of surface defects, which is not desirable in the case of MO removal because they will act as recombination centers for the charge carriers and inhibit photocatalytic performance. The band gap values of the $\text{WO}_3\text{-AMT-HF+P25}$ and $\text{WO}_3\text{-AMT-HCl+P25}$ composites were 3.10 and 3.01 eV, and they are photoactive under UV light irradiation; these samples generated the highest photocatalytic performance, hence evidencing the fact that the MC phase was advantageous for MO degradation, but correspondingly that there should be a well-defined equilibrium between the HPH and MC crystal phase's presence in the material. The optimum ratio seems to be around 87.5:12.5 (HPH to MC), which is very close to the 89:11 anatase rutile ratio in TiO_2 .

All WO_3 samples from each series exhibited inhibition on TiO_2 photocatalytic activity, except for the $\text{WO}_3\text{-AMT-HF}$ and $\text{WO}_3\text{-AMT-Cl}$ samples. Despite having different crystal phases and varying percentages of W^{5+} , both samples increased the TiO_2 photocatalytic activity. The $\text{WO}_3\text{-AMT-HF}$ sample with the hexagonal phase has the highest percentage W^{5+} and the highest adsorption affinity to water. In composite with TiO_2 , it reached the best conversion. The $\text{WO}_3\text{-AMT-Cl}$ sample, presenting an MC phase, also enhanced the TiO_2 photocatalytic performance. However, its abundance in the W^{5+} component is relatively low as compared to the other samples.

This study proves that the synthesis design of a WO_3 and $\text{WO}_3\cdot 0.33\text{H}_2\text{O}$ semiconductors is an essential issue, because a simple method such as substitution of the halide salts or the hydrohalic acids in the synthesis environment can result in a quasi-linear improvement of the photocatalytic activity (an activity that proved to be electronegativity dependent) in composite systems with P25. The systematic alternation of the shaping agents (in this case halide salts/hydrohalic acids) is a very important aspect of the semicon-

ductors' synthesis design because their cations and anions can affect the semiconductors' structure by intercalation. This intercalation in turn affects the morphology, crystal phase, crystal phase composition, lattice strain, water adsorption, and surface defects of the WO_3 and $\text{WO}_3 \cdot 0.33\text{H}_2\text{O}$ samples. By alternating the shaping agents in the function of their electronegativity, the photocatalytic activity of WO_3 and $\text{WO}_3 \cdot 0.33\text{H}_2\text{O}$ semiconductors in composite systems with P25 can be fine-tuned.

Supplementary Materials: The following are available online at <https://www.mdpi.com/article/10.3390/catal11070779/s1>, Figure S1: SEM micrographs of WO_3 -NWH-NaF and WO_3 -NWH-NaCl, Figure S2: SEM micrographs of WO_3 -NWH-NaBr and WO_3 -NWH-NaI, Figure S3: SEM micrographs of WO_3 -NWH-KCl, Figure S4: SEM micrographs of WO_3 -NWH-KBr and WO_3 -NWH-KI, Figure S5: SEM micrographs of WO_3 -AMT-HF and WO_3 -AMT-HCl, Figure S6: SEM micrographs of WO_3 -AMT-HBr and WO_3 -AMT-HI, Figure S7: The UV-Vis reflectance spectra of the WO_3 -NWH-NaX series, Figure S8: The UV-Vis reflectance spectra of the WO_3 -NWH-NaX+P25 composite series, Figure S9: The UV-Vis reflectance spectra of the WO_3 -NWH-KX series, Figure S10: The UV-Vis reflectance spectra of the WO_3 -NWH-KX+P25 composite series, Figure S11: The UV-Vis reflectance spectra of the WO_3 -AMT-HX series, Figure S12: The UV-Vis reflectance spectra of the WO_3 -NWH-KX+P25 composite series, Table S1: Electronegativity of the applied cations and anions and their corresponding acids/salts, Table S2: Distribution of W, O, Na, K, and C species in percentage from the XPS spectra for each synthesized semiconductor.

Author Contributions: Conceptualization, Z.P. and I.S.; methodology, I.S., E.-Z.K., Z.P. and M.B.; formal analysis, M.B.; investigation, I.S. and E.-Z.K.; resources, M.B. and Z.P.; writing—original draft preparation, I.S. and E.-Z.K.; writing—review and editing, Z.P. and M.B.; visualization, I.S.; supervision, Z.P. and M.B.; project administration, M.B. and Z.P.; funding acquisition, M.B. and Z.P. All authors have read and agreed to the published version of the manuscript.

Funding: This research was funded by Romanian National Authority for Scientific Research, CNCS-UEFISCDI, project number PN-III-P1-1.1-TE-2016-1588. I. Székely and E.-Zs. Kedves acknowledge the funding provided by the Sapientia Hungariae Foundation “Collegium Talentum” scholarship and by the Hungarian Academy of Sciences “Domus Junior” scholarship. Z. Pap acknowledges the financial support of the Bolyai János fellowship.

Institutional Review Board Statement: Not applicable.

Informed Consent Statement: Not applicable.

Data Availability Statement: Data is contained within the article, respectively, within the Supplementary Materials.

Acknowledgments: The authors wish to thank Tamás Gyulavári for the SEM micrographs and Klára Magyari for the XRD measurements. The authors express their gratitude to Tünde Székely for proofreading and addressing the manuscript's sentence and grammar errors.

Conflicts of Interest: The authors declare no conflict of interest.

References

1. Patnaik, P. *Handbook of Inorganic Chemicals*; McGraw Hill: New York, NY, USA, 2003; Volume 40, ISBN 0070494398.
2. Urasinska-Wojcik, B.; Vincent, T.A.; Chowdhury, M.; Gardner, J.W. Ultrasensitive WO_3 gas sensors for NO_2 detection in air and low oxygen environment. *Sens. Actuators B Chem.* **2017**, *239*, 1051–1059. [[CrossRef](#)]
3. Dong, C.; Zhao, R.; Yao, L.; Ran, Y.; Zhang, X.; Wang, Y. A review on WO_3 based gas sensors: Morphology control and enhanced sensing properties. *J. Alloy. Compd.* **2020**, *820*, 153194. [[CrossRef](#)]
4. Wang, Z.; Fan, X.; Li, C.; Men, G.; Han, D.; Gu, F. Humidity-Sensing Performance of 3DOM WO_3 with Controllable Structural Modification. *ACS Appl. Mater. Interfaces* **2018**, *10*, 3776–3783. [[CrossRef](#)]
5. Bogati, S.; Georg, A.; Graf, W. Photoelectrochromic devices based on sputtered WO_3 and TiO_2 films. *Sol. Energy Mater. Sol. Cells* **2017**, *163*, 170–177. [[CrossRef](#)]
6. Bae, J.; Kim, H.; Moon, H.C.; Kim, S.H. Low-voltage, simple WO_3 -based electrochromic devices by directly incorporating an anodic species into the electrolyte. *J. Mater. Chem. C* **2016**, *4*, 10887–10892. [[CrossRef](#)]
7. Cossari, P.; Pugliese, M.; Simari, C.; Mezzi, A.; Maiorano, V.; Nicotera, I.; Gigli, G. Simplified All-Solid-State WO_3 Based Electrochromic Devices on Single Substrate: Toward Large Area, Low Voltage, High Contrast, and Fast Switching Dynamics. *Adv. Mater. Interfaces* **2020**, *7*. [[CrossRef](#)]

8. Yun, T.Y.; Li, X.; Bae, J.; Kim, S.H.; Moon, H.C. Non-volatile, Li-doped ion gel electrolytes for flexible WO₃-based electrochromic devices. *Mater. Des.* **2019**, *162*, 45–51. [[CrossRef](#)]
9. Bazarjani, M.S.; Hojamberdiev, M.; Morita, K.; Zhu, G.; Cherkashinin, G.; Fasel, C.; Herrmann, T.; Breitzke, H.; Gurlo, A.; Riedel, R. Visible Light Photocatalysis with c-WO₃-x/WO₃ × H₂O Nanoheterostructures In Situ Formed in Mesoporous Polycarbosilane-Siloxane Polymer. *J. Am. Chem. Soc.* **2013**, *135*, 4467–4475. [[CrossRef](#)]
10. Liu, Q.; Wang, F.; Lin, H.; Xie, Y.; Tong, N.; Lin, J.; Zhang, X.; Zhang, Z.; Wang, X. Surface oxygen vacancy and defect engineering of WO₃ for improved visible light photocatalytic performance. *Catal. Sci. Technol.* **2018**, *8*, 4399–4406. [[CrossRef](#)]
11. Shang, J.; Xiao, Z.; Yu, L.; Aprea, P.; Hao, S. An insight on the role of PVP in the synthesis of monoclinic WO₃ with efficiently photocatalytic activity. *Nanotechnology* **2019**, *31*, 125603. [[CrossRef](#)]
12. Baia, L.; Orbán, E.; Fodor, S.; Hampel, B.; Kedves, E.Z.; Saszet, K.; Székely, I.; Karácsonyi, É.; Réti, B.; Berki, P.; et al. Preparation of TiO₂/WO₃ composite photocatalysts by the adjustment of the semiconductors' surface charge. *Mater. Sci. Semicond. Process.* **2016**, *42*, 66–71. [[CrossRef](#)]
13. Kokorin, A.I.; Sviridova, T.V.; Konstantinova, E.A.; Sviridov, D.V.; Bahnemann, D.W. Dynamics of Photogenerated Charge Carriers in TiO₂/MoO₃, TiO₂/WO₃ and TiO₂/V₂O₅ Photocatalysts with Mosaic Structure. *Catalysts* **2020**, *10*, 1022. [[CrossRef](#)]
14. Fernández-Domene, R.; Sánchez-Tovar, R.; Lucas-Granados, B.; Roselló-Márquez, G.; Garcia-Anton, J. A simple method to fabricate high-performance nanostructured WO₃ photocatalysts with adjusted morphology in the presence of complexing agents. *Mater. Des.* **2017**, *116*, 160–170. [[CrossRef](#)]
15. Chen, P.; Qin, M.; Chen, Z.; Jia, B.; Zhao, S.; Wan, Q.; Qu, X. A novel approach to synthesize the amorphous carbon-coated WO₃ with defects and excellent photocatalytic properties. *Mater. Des.* **2016**, *106*, 22–29. [[CrossRef](#)]
16. Wu, C.-M.; Naseem, S.; Chou, M.-H.; Wang, J.-H.; Jian, Y.-Q. Recent Advances in Tungsten-Oxide-Based Materials and Their Applications. *Front. Mater.* **2019**, *6*, 6. [[CrossRef](#)]
17. Li, S.; Hu, S.; Jiang, W.; Zhang, J.; Xu, K.; Wang, Z. In situ construction of WO₃ nanoparticles decorated Bi₂MoO₆ microspheres for boosting photocatalytic degradation of refractory pollutants. *J. Colloid Interface Sci.* **2019**, *556*, 335–344. [[CrossRef](#)] [[PubMed](#)]
18. Wei, S.; Zhao, G.; Du, W.; Tian, Q. Synthesis and excellent acetone sensing properties of porous WO₃ nanofibers. *Vacuum* **2016**, *124*, 32–39. [[CrossRef](#)]
19. Jeong, K.; Lee, J.; Byun, I.; Seong, M.-J.; Park, J.; Nam, H.-S.; Lee, J. Pulsed laser chemical vapor deposition of a mixture of W, WO₂, and WO₃ from W(CO)₆ at atmospheric pressure. *Thin Solid Films* **2017**, *626*, 145–153. [[CrossRef](#)]
20. Ito, A.; Morishita, Y. Selective self-oriented growth of (2 0 0), (0 0 2), and (0 2 0) δ-WO₃ films via metal-organic chemical vapor deposition. *Mater. Lett.* **2020**, *258*, 126817. [[CrossRef](#)]
21. Verma, M.; Singh, K.P.; Kumar, A. Reactive magnetron sputtering based synthesis of WO₃ nanoparticles and their use for the photocatalytic degradation of dyes. *Solid State Sci.* **2020**, *99*, 105847. [[CrossRef](#)]
22. Fan, G.; Chen, D.; Li, T.; Yi, S.; Ji, H.; Wang, Y.; Zhang, Z.; Shao, G.; Fan, B.; Wang, H.; et al. Enhanced room-temperature ammonia-sensing properties of polyaniline-modified WO₃ nanoplates derived via ultrasonic spray process. *Sens. Actuators B Chem.* **2020**, *312*, 127892. [[CrossRef](#)]
23. Govender, M.; Shikwambana, L.; Mwakikunga, B.W.; Sideras-Haddad, E.; Erasmus, R.M.; Forbes, A. Formation of tungsten oxide nanostructures by laser pyrolysis: Stars, fibres and spheres. *Nanoscale Res. Lett.* **2011**, *6*, 166. [[CrossRef](#)] [[PubMed](#)]
24. Park, S.-M.; Nah, Y.-C.; Nam, C. Effects of Hydrothermal Treatment Duration on Morphology of WO₃ Nanostructures. *J. Nanosci. Nanotechnol.* **2017**, *17*, 7719–7722. [[CrossRef](#)]
25. Li, Z.; Zhou, Y.; Yao, Q.; Wang, W.; Wang, H.; Wang, D.; Liu, X.; Xu, J. Facile synthesis of WO₃ nanocuboids from tungsten trioxide powder and hydrogen peroxide. *Mater. Lett.* **2019**, *236*, 197–200. [[CrossRef](#)]
26. Li, N.; Chang, T.; Gao, H.; Gao, X.; Ge, L. Morphology-controlled WO₃-x homojunction: Hydrothermal synthesis, adsorption properties, and visible-light-driven photocatalytic and chromic properties. *Nanotechnology* **2019**, *30*, 415601. [[CrossRef](#)]
27. Liu, D.; Ren, X.; Li, Y.; Tang, Z.; Zhang, Z. Nanowires-assembled WO₃ nanomesh for fast detection of ppb-level NO₂ at low temperature. *J. Adv. Ceram.* **2020**, *9*, 17–26. [[CrossRef](#)]
28. Zeb, S.; Peng, X.; Yuan, G.; Zhao, X.; Qin, C.; Sun, G.; Nie, Y.; Cui, Y.; Jiang, X. Controllable synthesis of ultrathin WO₃ nanotubes and nanowires with excellent gas sensing performance. *Sens. Actuators B Chem.* **2020**, *305*, 127435. [[CrossRef](#)]
29. Lu, N.; Gao, X.; Yang, C.; Xiao, F.; Wang, J.; Su, X. Enhanced formic acid gas-sensing property of WO₃ nanorod bundles via hydrothermal method. *Sens. Actuators B Chem.* **2016**, *223*, 743–749. [[CrossRef](#)]
30. Ryu, S.-M.; Nam, C. Adsorption Characteristics of Methylene Blue on WO₃ Nanorods Prepared by Microwave-Assisted Hydrothermal Methods. *Phys. Status Solidi A* **2018**, *215*, 1700996. [[CrossRef](#)]
31. Cao, S.; Zhao, C.; Han, T.; Peng, L. Hydrothermal synthesis, characterization and gas sensing properties of the WO₃ nanofibers. *Mater. Lett.* **2016**, *169*, 17–20. [[CrossRef](#)]
32. Yao, S.; Zheng, X.; Zhang, X.; Xiao, H.; Qu, F.; Wu, X. Facile synthesis of flexible WO₃ nanofibers as supercapacitor electrodes. *Mater. Lett.* **2017**, *186*, 94–97. [[CrossRef](#)]
33. Shen, Y.; Pan, L.; Ren, Z.; Yang, Y.; Xiao, Y.; Li, Z. Nanostructured WO₃ films synthesized on mica substrate with novel photochromic properties. *J. Alloy. Compd.* **2016**, *657*, 450–456. [[CrossRef](#)]
34. Zhou, J.; Lin, S.; Chen, Y.; Gaskov, A. Facile morphology control of WO₃ nanostructure arrays with enhanced photoelectrochemical performance. *Appl. Surf. Sci.* **2017**, *403*, 274–281. [[CrossRef](#)]

35. Adhikari, S.; Chandra, K.S.; Kim, D.-H.; Madras, G.; Sarkar, D. Understanding the morphological effects of WO₃ photocatalysts for the degradation of organic pollutants. *Adv. Powder Technol.* **2018**, *29*, 1591–1600. [[CrossRef](#)]
36. Ghasemi, L.; Jafari, H. Morphological Characterization of Tungsten Trioxide Nanopowders Synthesized by Sol-Gel Modified Pechini's Method. *Mater. Res.* **2017**, *20*, 1713–1721. [[CrossRef](#)]
37. Tahir, M.B.; Nabi, G.; Khalid, N.R.; Khan, W.S. Synthesis of Nanostructured Based WO₃ Materials for Photocatalytic Applications. *J. Inorg. Organomet. Polym. Mater.* **2017**, *28*, 777–782. [[CrossRef](#)]
38. Zhang, D.; Fan, Y.; Li, G.; Ma, Z.; Wang, X.; Cheng, Z.; Xu, J. Highly sensitive BTEX sensors based on hexagonal WO₃ nanosheets. *Sensors Actuators B: Chem.* **2019**, *293*, 23–30. [[CrossRef](#)]
39. Fan, Y.; Xi, X.; Liu, Y.; Nie, Z.; Zhang, Q.; Zhao, L. Growth mechanism of immobilized WO₃ nanostructures in different solvents and their visible-light photocatalytic performance. *J. Phys. Chem. Solids* **2020**, *140*, 109380. [[CrossRef](#)]
40. Wang, C.; Ding, M.; Kou, X.; Guo, L.; Feng, C.; Li, X.; Zhang, H.; Sun, P.; Sun, Y.; Lu, G. Detection of nitrogen dioxide down to ppb levels using flower-like tungsten oxide nanostructures under different annealing temperatures. *J. Colloid Interface Sci.* **2016**, *483*, 314–320. [[CrossRef](#)] [[PubMed](#)]
41. Pudukudy, M.; Jia, Q. Facile chemical synthesis of nanosheets self-assembled hierarchical H₂WO₄ microspheres and their morphology-controlled thermal decomposition into WO₃ microspheres. *J. Mater. Sci.* **2019**, *54*, 13914–13937. [[CrossRef](#)]
42. Kožakova, Z.; Mrlik, M.; Sedlačik, M.; Pavlinek, V.; Kuritka, I. Preparation of TiO₂ powder by microwave-assisted molten-salt synthesis. In Proceedings of the NANOCON 2011, 3rd International Conference, Brno, Czech Republic, 21–23 September 2011; pp. 345–351.
43. Putri, I.E.; Budiarti, H.A.; Sawitri, D.; Risanti, D.D. On the Role of NaCl Addition to Phase Transformation of TiO₂ from TiCl₃. *Adv. Mater. Res.* **2015**, *1112*, 313–316. [[CrossRef](#)]
44. Yin, H.; Wada, Y.; Kitamura, T.; Sumida, T.; Hasegawa, Y.; Yanagida, S. Novel synthesis of phase-pure nano-particulate anatase and rutile TiO₂ using TiCl₄ aqueous solutions. *J. Mater. Chem.* **2001**, *12*, 378–383. [[CrossRef](#)]
45. Kaur, M.; Kalia, A. Role of salt precursors for the synthesis of zinc oxide nanoparticles and in imparting variable antimicrobial activity. *J. Appl. Nat. Sci.* **2016**, *8*, 1039–1048. [[CrossRef](#)]
46. Pourrahimi, A.M.; Liu, D.; Pallon, L.K.H.; Andersson, R.L.; Abad, A.M.; Lagarón, J.-M.; Hedenqvist, M.S.; Ström, V.; Gedde, U.W.; Olsson, R.T. Water-based synthesis and cleaning methods for high purity ZnO nanoparticles—Comparing acetate, chloride, sulphate and nitrate zinc salt precursors. *RSC Adv.* **2014**, *4*, 35568–35577. [[CrossRef](#)]
47. Zheng, Y.-Z.; Zhang, M.-L. Preparation and electrochemical properties of nickel oxide by molten-salt synthesis. *Mater. Lett.* **2007**, *61*, 3967–3969. [[CrossRef](#)]
48. Phuruangrat, A.; Ham, D.J.; Hong, S.J.; Thongtem, S.; Lee, J.S. Synthesis of hexagonal WO₃ nanowires by microwave-assisted hydrothermal method and their electrocatalytic activities for hydrogen evolution reaction. *J. Mater. Chem.* **2010**, *20*, 1683–1690. [[CrossRef](#)]
49. Chen, L.; Lam, S.; Zeng, Q.; Amal, R.; Yu, A. Effect of Cation Intercalation on the Growth of Hexagonal WO₃ Nanorods. *J. Phys. Chem. C* **2012**, *116*, 11722–11727. [[CrossRef](#)]
50. Uresti, D.B.H.; Martínez, D.S.; la Cruz, A.M.-D.; Sepulveda-Guzman, S.; Torres-Martínez, L.M. Characterization and photocatalytic properties of hexagonal and monoclinic WO₃ prepared via microwave-assisted hydrothermal synthesis. *Ceram. Int.* **2014**, *40*, 4767–4775. [[CrossRef](#)]
51. Kang, M.; Liang, J.; Wang, F.; Chen, X.; Lu, Y.; Zhang, J. Structural design of hexagonal/monoclinic WO₃ phase junction for photocatalytic degradation. *Mater. Res. Bull.* **2020**, *121*, 110614. [[CrossRef](#)]
52. Wang, J.-C.; Shi, W.; Sun, X.-Q.; Wu, F.-Y.; Li, Y.; Hou, Y. Enhanced Photo-Assisted Acetone Gas Sensor and Efficient Photocatalytic Degradation Using Fe-Doped Hexagonal and Monoclinic WO₃ Phase—Junction. *Nanomaterials* **2020**, *10*, 398. [[CrossRef](#)]
53. Xu, Y.; Schoonen, M.A. The absolute energy positions of conduction and valence bands of selected semiconducting minerals. *Am. Miner.* **2000**, *85*, 543–556. [[CrossRef](#)]
54. Ali, H.; Guler, A.; Masar, M.; Urbanek, P.; Urbanek, M.; Skoda, D.; Suly, P.; Machovsky, M.; Galusek, D.; Kuritka, I. Solid-State Synthesis of Direct Z-Scheme Cu₂O/WO₃ Nanocomposites with Enhanced Visible-Light Photocatalytic Performance. *Catalysts* **2021**, *11*, 293. [[CrossRef](#)]
55. Liu, X.; Zhang, J.; Yang, T.; Guo, X.; Wu, S.; Wang, S. Synthesis of Pt nanoparticles functionalized WO₃ nanorods and their gas sensing properties. *Sens. Actuators B Chem.* **2011**, *156*, 918–923. [[CrossRef](#)]
56. Xiang, Q.; Meng, G.F.; Zhao, H.B.; Zhang, Y.; Li, H.; Ma, W.J.; Xu, J.Q. Au Nanoparticle Modified WO₃ Nanorods with Their Enhanced Properties for Photocatalysis and Gas Sensing. *J. Phys. Chem. C* **2010**, *114*, 2049–2055. [[CrossRef](#)]
57. Pfeifer, J.; Guifang, C.; Tekula-Buxbaum, P.; Kiss, B.; Farkas-Jahnke, M.; Vadasdi, K. A reinvestigation of the preparation of tungsten oxide hydrate WO₃ · 1/3H₂O. *J. Solid State Chem.* **1995**, *119*, 90–97. [[CrossRef](#)]
58. Mattoni, G.; Filippetti, A.; Manca, N.; Zubko, P.; Caviglia, A.D. Charge doping and large lattice expansion in oxygen-deficient heteroepitaxial WO₃. *Phys. Rev. Mater.* **2018**, *2*, 053402. [[CrossRef](#)]
59. Lethy, K.; Beena, D.; Kumar, R.; Pillai, V.M.; Ganesan, V.; Sathe, V. Structural, optical and morphological studies on laser ablated nanostructured WO₃ thin films. *Appl. Surf. Sci.* **2008**, *254*, 2369–2376. [[CrossRef](#)]

60. Li, J.; Guo, H.; Feng, X. Nanorod-Assembled WO₃-0.33H₂O Microstructures with Improved Photocatalytic Property. *Chin. J. Appl. Chem.* **2017**, *34*, 60–70.
61. Kumar, N.; Kumbhat, S. *Concise Concepts of Nanoscience and Nanomaterials*; Scientific Publishers: Singapore, 2018; ISBN 9789388172066.
62. Lee, S.-H.; Cheong, H.M.; Liu, P.; Smith, D.; Tracy, C.; Mascarenhas, A.; Pitts, J.R.; Deb, S.K. Raman spectroscopic studies of gasochromic a-WO₃ thin films. *Electrochimica Acta* **2001**, *46*, 1995–1999. [[CrossRef](#)]
63. Singh, D.M.D.J.; Pradeep, T.; Thirumoorthy, K.; Balasubramanian, K. Closed-Cage Tungsten Oxide Clusters in the Gas Phase. *J. Phys. Chem. A* **2010**, *114*, 5445–5452. [[CrossRef](#)] [[PubMed](#)]
64. Stankova, N.; Atanasov, P.; Stanimirova, T.; Dikovska, A.O.; Eason, R. Thin (001) tungsten trioxide films grown by laser deposition. *Appl. Surf. Sci.* **2005**, *247*, 401–405. [[CrossRef](#)]
65. De Wijs, G.; De Groot, R. Amorphous WO₃: A first-principles approach. *Electrochimica Acta* **2001**, *46*, 1989–1993. [[CrossRef](#)]
66. Yan, H.; Tian, C.; Sun, L.; Wang, B.; Wang, L.; Yin, J.; Wu, A.; Fu, H. Small-sized and high-dispersed WN from [SiO₄(W₃O₉)₄]⁴⁻ clusters loading on GO-derived graphene as promising carriers for methanol electro-oxidation. *Energy Environ. Sci.* **2014**, *7*, 1939–1949. [[CrossRef](#)]
67. Garcia-Sanchez, R.F.; Ahmido, T.; Casimir, D.; Baliga, S.; Misra, P. Thermal Effects Associated with the Raman Spectroscopy of WO₃Gas-Sensor Materials. *J. Phys. Chem. A* **2013**, *117*, 13825–13831. [[CrossRef](#)] [[PubMed](#)]
68. Tägtström, P.; Jansson, U. Chemical vapour deposition of epitaxial WO₃ films. *Thin Solid Films* **1999**, *352*, 107–113. [[CrossRef](#)]
69. Daniel, M.; Desbat, B.; Lassegues, J.; Gerand, B.; Figlarz, M. Infrared and Raman study of WO₃ tungsten trioxides and WO₃·xH₂O tungsten trioxide hydrates. *J. Solid State Chem.* **1987**, *67*, 235–247. [[CrossRef](#)]
70. Selvakumar, D.; Nagaraju, P.; Jayavel, R. Graphene-metal oxide based nanocomposites for supercapacitor applications. *TechConnect Briefs* **2018**, *1*, 70–73.
71. Cremonesi, A.; Bersani, D.; Lottici, P.P.; Djaoued, Y.; Ashrit, P. WO₃ thin films by sol–gel for electrochromic applications. *J. Non-Crystalline Solids* **2004**, *345-346*, 500–504. [[CrossRef](#)]
72. Wolcott, A.; Kuykendall, T.R.; Chen, W.; Chen, A.S.; Zhang, J.Z. Synthesis and Characterization of Ultrathin WO₃Nanodisks Utilizing Long-Chain Poly(ethylene glycol). *J. Phys. Chem. B* **2006**, *110*, 25288–25296. [[CrossRef](#)] [[PubMed](#)]
73. Braun, A.; Akgul, F.A.; Chen, Q.; Erat, S.; Huang, T.-W.; Jabeen, N.; Liu, Z.; Mun, B.S.; Mao, S.S.; Zhang, X. Observation of Substrate Orientation-Dependent Oxygen Defect Filling in Thin WO₃-δ/TiO₂ Pulsed Laser-Deposited Films with in Situ XPS at High Oxygen Pressure and Temperature. *Chem. Mater.* **2012**, *24*, 3473–3480. [[CrossRef](#)]
74. Shpak, A.; Korduban, A.; Medvedskij, M.; Kandyba, V. XPS studies of active elements surface of gas sensors based on WO₃-x nanoparticles. *J. Electron Spectrosc. Relat. Phenom.* **2007**, *156-158*, 172–175. [[CrossRef](#)]
75. Leghari, S.A.K.; Sajjad, S.; Chen, F.; Zhang, J. WO₃/TiO₂ composite with morphology change via hydrothermal template-free route as an efficient visible light photocatalyst. *Chem. Eng. J.* **2011**, *166*, 906–915. [[CrossRef](#)]
76. Paula, L.F.; Hofer, M.; Lacerda, V.P.B.; Bahnemann, D.W.; Patrocinio, A.O.T. Unraveling the photocatalytic properties of TiO₂/WO₃ mixed oxides. *Photochem. Photobiol. Sci.* **2019**, *18*, 2469–2483. [[CrossRef](#)] [[PubMed](#)]
77. Rahimnejad, S.; He, J.H.; Pan, F.; Lee, X.; Chen, W.; Wu, K.; Xu, G.Q. Enhancement of the photocatalytic efficiency of WO₃ nanoparticles via hydrogen plasma treatment. *Mater. Res. Express* **2014**, *1*. [[CrossRef](#)]
78. Yang, F.; Jia, J.; Mi, R.; Liu, X.; Fu, Z.; Wang, C.; Liu, X.; Tang, Y. Fabrication of WO₃-2H₂O/BC Hybrids by the Radiation Method for Enhanced Performance Supercapacitors. *Front. Chem.* **2018**, *6*, 290. [[CrossRef](#)] [[PubMed](#)]
79. Nayak, A.K.; Das, A.K.; Pradhan, D. High Performance Solid-State Asymmetric Supercapacitor using Green Synthesized Graphene-WO₃ Nanowires Nanocomposite. *ACS Sustain. Chem. Eng.* **2017**, *5*, 10128–10138. [[CrossRef](#)]
80. Cole, B.; Marsen, B.; Miller, E.; Yan, Y.; To, B.; Jones, K.; Al-Jassim, M. Evaluation of Nitrogen Doping of Tungsten Oxide for Photoelectrochemical Water Splitting. *J. Phys. Chem. C* **2008**, *112*, 5213–5220. [[CrossRef](#)]
81. Solarska, R.; Alexander, B.; Braun, A.; Jurczakowski, R.; Fortunato, G.; Stiefel, M.; Graule, T.; Augustynski, J. Tailoring the morphology of WO₃ films with substitutional cation doping: Effect on the photoelectrochemical properties. *Electrochimica Acta* **2010**, *55*, 7780–7787. [[CrossRef](#)]
82. Székely, I.; Baia, M.; Magyari, K.; Boga, B.; Pap, Z. The effect of the pH adjustment upon the WO₃-WO₃·0.33H₂O-TiO₂ ternary composite systems' photocatalytic activity. *Appl. Surf. Sci.* **2019**, *490*, 469–480. [[CrossRef](#)]
83. Nie, C.; Dong, J.; Sun, P.; Yan, C.; Wu, H.; Wang, B. An efficient strategy for full mineralization of an azo dye in wastewater: A synergistic combination of solar thermo- and electrochemistry plus photocatalysis. *RSC Adv.* **2017**, *7*, 36246–36255. [[CrossRef](#)]
84. Karácsonyi, É.; Baia, L.; Dombi, A.; Danciu, V.; Mogyorósi, K.; Pop, L.; Kovács, G.; Coşoveanu, V.; Vulpoi, A.; Simon, S.; et al. The photocatalytic activity of TiO₂/WO₃/noble metal (Au or Pt) nanoarchitectures obtained by selective photodeposition. *Catal. Today* **2013**, *208*, 19–27. [[CrossRef](#)]
85. Székely, I.; Kovács, G.; Baia, L.; Danciu, V.; Pap, Z. Synthesis of Shape-Tailored WO₃ Micro-/Nanocrystals and the Photocatalytic Activity of WO₃/TiO₂ Composites. *Materials* **2016**, *9*, 258. [[CrossRef](#)] [[PubMed](#)]
86. Boga, B.; Székely, I.; Pap, Z.; Baia, L.; Baia, M. Detailed Spectroscopic and Structural Analysis of TiO₂/WO₃ Composite Semiconductors. *J. Spectrosc.* **2018**, *2018*, 1–7. [[CrossRef](#)]
87. Kedves, E.-Z.; Székely, I.; Baia, L.; Baia, M.; Csavdári, A.; Pap, Z. The Comparison of the Photocatalytic Performance Shown by TiO₂ and TiO₂/WO₃ Composites—A Parametric and Kinetic Study. *J. Nanosci. Nanotechnol.* **2019**, *19*, 356–365. [[CrossRef](#)]

-
88. Matthews, F. Specimen preparation. *Mech. Test. Adv. Fibre Compos.* **2000**, *138*, 36–42. [[CrossRef](#)]
 89. Kubelka, P.; Munk, K. The Kubelka-Munk Theory of Reflectance. *Zeit. Für Tekn. Phys.* **1931**, *12*, 539.
 90. Veréb, G.; Manczinger, L.; Bozsó, G.; Sienkiewicz, A.; Forró, L.; Mogyorósi, K.; Hernádi, K.; Dombi, A. Comparison of the photocatalytic efficiencies of bare and doped rutile and anatase TiO₂ photocatalysts under visible light for phenol degradation and E. coli inactivation. *Appl. Catal. B Environ.* **2013**, *129*, 566–574. [[CrossRef](#)]